Investigating Particle Properties of Saturn's Narrow Rings from Diffraction Reconstructed Profiles Obtained from Cassini Radio Science

Advaith Mopuri[1] And Maggie Shen[2]
MIT PRIMES-USA

[1] *Mission San Jose High School, Fremont, CA*
[2] *Leland High School, San Jose, CA*

(Dated: February 17, 2026)

ABSTRACT

The Cassini mission's Radio Science Subsystem (RSS) conducted occultation observations of the rings by transmitting coherent radiation at wavelengths of 0.94cm (Ka band), 3.6cm (X band), and 13cm (S band) into several Deep Space Networks (DSNs) across the globe. Diffraction effects for each band are primarily caused by particles comparable in size to their wavelengths. As such, comparing the wavelength dependence of optical depth to values predicted by Mie scattering theory allows us to constrain the power-law size distribution of particles in Saturn's rings. We utilize a novel high-resolution reconstruction method to obtain the diffraction-corrected optical depth of narrow ringlets at 3 wavelengths. From these measurements, we infer that there are significant regional differences in size distributions throughout various narrow ringlets, which may hold clues about their varying dynamical environments. In particular, we identify differences in particle size distributions between the F ring, the structurally similar Strange ringlet, and the C ring plateaus. Our results indicate that the F ring properties are different from those of other ring regions, which may be related to the speculated clumpy nature of the F ring itself.

Keywords: Diffraction, Mie scattering, narrow ringlets, particle sizes, radio occultation, Saturn's rings.

1. INTRODUCTION

Among Saturn's rich and varied ring system, the F ring and other narrow rings stand apart in their structure and detailed orbits (Murray & French 2018). First detected in 1979 by the Pioneer 11 spacecraft, then imaged by the two Voyager flybys in the following two years (Colwell et al. 2009), the F ring was determined to be narrow with a radial width of roughly 50 kilometers and multiple-stranded. The Photopolarimeter System (PPS) on Voyager 2 also showed that the F ring contained a narrow, $<$ 3km wide, optically thick (of optical depth $\tau \sim 1$) core surrounded by a sheet of dust (Murray & French 2018). The eccentric F ring is a complex dynamical environment with a satellite on either side affecting the ring's dynamics: Prometheus, which was found to intermittently shepherd the F ring (Cuzzi et al. 2024), and Pandora. Stellar and radio occultations from the Cassini mission reveal this ring to be a particularly interesting and varied system.

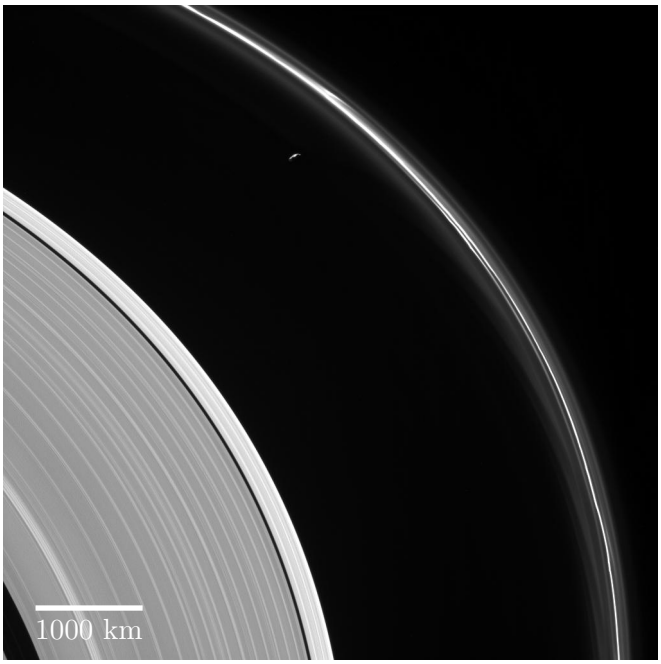

(1a) The F ring and a thin sliver of its shepherding moon, Prometheus. The ring's faint and wispy features seen in this image result from Prometheus' gravitational pull. The image scale is 6 kilometers per pixel.

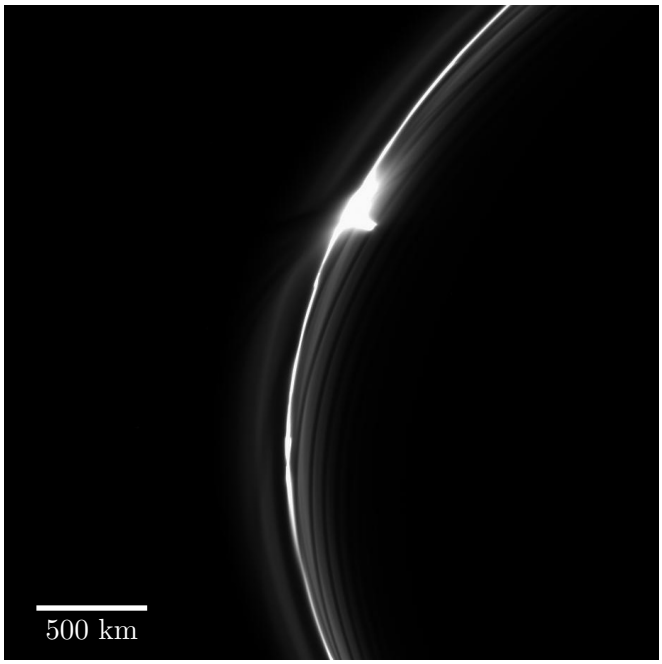

(1b) A variety of features visible in the F ring: a bright clump, "gores" to the right of the bright clump, and a "jet" to the left of the bright clump. The image scale is 2.9 kilometers per pixel.

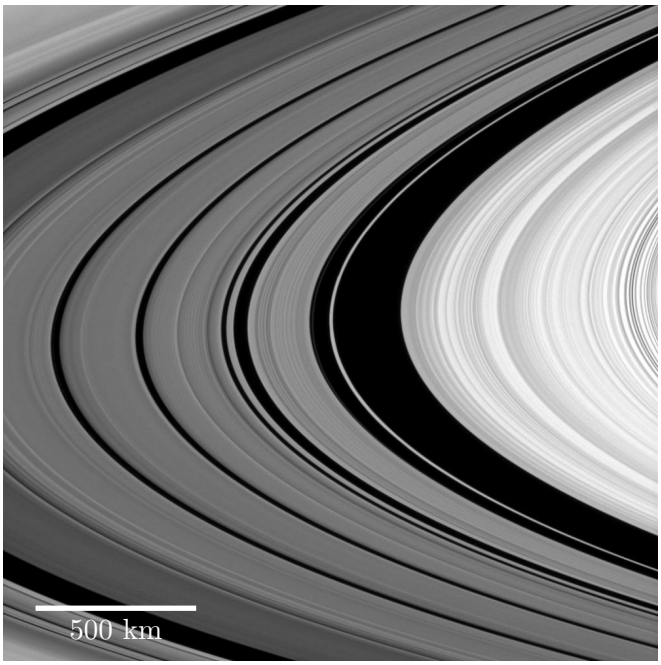

(1c) The Cassini Division occupies most of this image and contains five dim bands of ring material. The B ring lies to the right. The largest dark band is the Huygens Gap, which contains the Strange ringlet. The image scale is 2 kilometers per pixel.

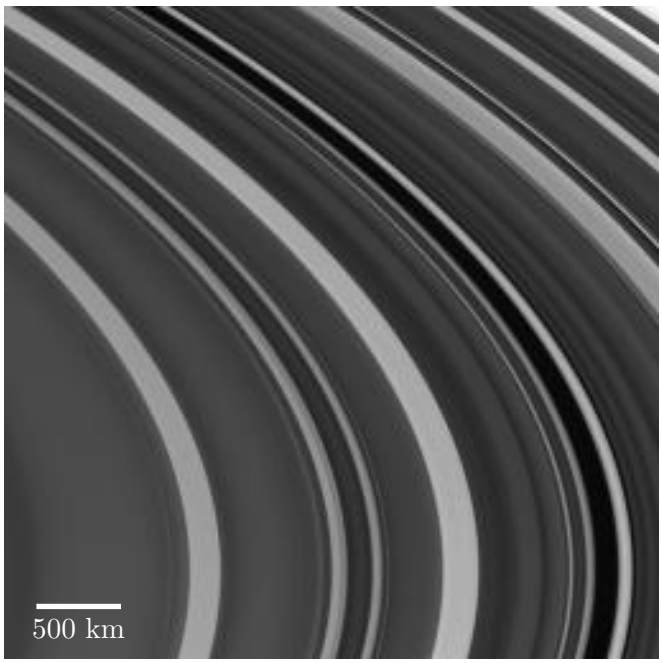

(1d) Plateaus—bright regions unique to the C ring—and gaps are visible in the outer C ring. The dark gap through the center of the image contains the Maxwell Ringlet. The image scale is 4.6 kilometers per pixel.

Figure 1. Images of Saturn's rings captured by Cassini ISS using the narrow angle camera. Image credit: NASA/JPL-Caltech (2004–2017).

Prior studies have offered significant insight into the structure of the F ring. Cassini images and stellar occultations have shown that the F ring is dominated by tiny, micron-sized "dust" particles, leading researchers to predict that these particles are resupplied from unseen, more massive particles (Murray & French 2018). Additionally, "jets", thought to be caused by collisions between core material and surrounding objects, and transient clumps observed by the Cassini ISS (Imaging Subsystem) provided more evidence for large particles (Murray & French 2018). Cuzzi et al. (2024) found that although it is surrounded by dust, the F ring's mass is dominated by a true core less than 1 kilometer in radial width. They also showed that this true core is only intermittently detected by the Cassini RSS, and inferred that the core is asymmetric and structured as a chain of disconnected "arcs" in the same orbit. Furthermore, using star occultations from the Cassini Ultraviolet Imaging Spectrograph (UVIS), Esposito et al. (2008) found evidence for elongated clumps in the F ring core known as kittens. Albrebdi & Esposito (2025) refined this description by hypothesizing that the F ring's true core is made up of these kittens, a fraction of which are shepherded by Prometheus.

Though much is known, the F ring still has many mysteries and strange features. It is still unknown how the F ring is confined, and why kittens have formed. Due to its discontinuous nature, unique gravitational interactions with Prometheus, transient features, and narrowness, the F ring differs substantially from Saturn's other ring regions, which are generally broad and radially symmetric, making it a valuable target for further investigation.

In this paper, we utilize data from the Cassini Radio Science Subsystem (RSS) to analyze the structure of the F ring, as well as the similarly narrow (roughly 2km in radial width), eccentric, and inclined Strange ringlet. Specifically, we characterize particle size variations in these narrow rings and reveal differences in their structure and dynamical behavior. We develop a novel technique that allows us to obtain high-resolution diffraction-corrected reconstructions of the optical depth of these ring features at three different wavelengths: 0.94cm (Ka Band), 3.6cm (X Band), and 13cm (S Band). Each band can only detect particles comparable in size to its wavelength, so combining data from all three provides significant constraints on the size distribution of particles with radii on the order of millimeters to meters in Saturn's rings. In particular, this means we observe relatively larger ice particles and not micron-sized dust particles as in the case of UVIS or the Visible and Infrared Mapping Spectrometer (VIMS).

Constrained particle size distributions reveals a significant amount of detail about the ring itself. For example, we can calculate the surface density and the effective particle size in the ring, and combined with the porosity of particles in the ring, we can also find the mass of the ring itself. Finally, we can identify mesoscale structures within a ring, like self-gravity wakes, which are only one or a few orders of magnitude greater than the particles themselves. These interesting structures are especially present in narrow rings (like the F ring and Strange ringlet) due to their elliptical orbits and eccentric nature (French et al. 2016; Bosh et al. 2002), making their size distributions even more intriguing.

Similar analysis has been done on other ring regions; for instance, Jerousek et al. (2020) used data from UVIS, VIMS, and RSS to investigate the particle size distribution of the C ring plateaus and Cassini division. In addition to investigating the F ring and Strange ringlet, we also provide an analysis of the C ring plateaus due to their varied dynamical environments and in order to provide some comparison with Jerousek et al. (2020).

Section 2 provides a more detailed overview of RSS occultation observations, and describes the theory of reconstructing optical depth profiles from said observations. Next, in Section 3, we review Mie scattering theory and the relation between particle sizes and differential optical depth measurements. We also illustrate the sensitivity of the radio wavelengths utilized by the Cassini RSS to ring particles ranging from a few millimeters to a few meters in size. In Section 4, we present our results for particle size distributions in the F ring and compare it to particle size distributions in the Strange ringlet and C ring plateaus. We also compare our results to existing values of particle sizes in broader ring regions derived from ultraviolet and infrared wavelength stellar occultations rather than the longer radio wavelengths used by the Cassini RSS. Our results indicate significant differences between particle sizes in different ring features as well as deviations from standard power law size distributions in certain rings. We suggest possible interpretations for these differences based on our data, including our leading theory that the F ring contains significantly more particles a few millimeters in size than other ring regions due to frequent perturbations by Prometheus. Finally, in Section 5, we discuss the implications of our results and outline directions for future research.

2. CASSINI RADIO SCIENCE OBSERVATIONS

The Cassini Radio Science Subsystem (RSS) transmits coherent radiation at wavelengths of 0.94cm (Ka Band), 3.6cm (X Band), and 13cm (S Band) through Saturn's rings in an occultation geometry (Figure 3). The resulting diffraction pattern due to the rings is received by one of NASA's 34m or 70m Deep Space Network (DSN) antennas in California, Spain, and Australia, where both the power and phase of incoming radio signals are measured (Asmar et al. 2018). On their own, power measurements are diffraction limited: the signal is distorted by the effects of diffraction and thus the structure of the rings is obscured. Therefore, we use the difference in phase from the transmitted and incoming radio signals together with the power measurements to reconstruct a profile of the complex transmittance of the rings.

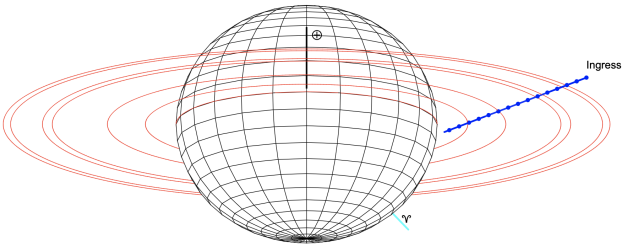

Figure 2. Occultation geometry of Rev 028. The tick marks along the blue line represent a constant time scale of one hour. The close spacing of tick marks indicates that the occultation was performed slowly from a long distance, which in turn implies a large Fresnel scale for diffraction effects due to the rings. Note how the occultation geometry covers all of the rings in high detail.

2.1. *Occultation Geometry*

The typical geometry of a radio occultation is shown in Figure 3 (see also Marouf et al. (1986), Fig. 1). The coordinate system we use is centered at Saturn; the x-y plane corresponds to the mean surface of the rings, while the z-axis runs through the north pole of Saturn. The unit vector $\hat{\boldsymbol{u}}_{\boldsymbol{i}}$ is directed along the line-of-sight from Earth to Saturn at the time of occultation. Since Cassini and Earth on opposite sides of the ring, the line-of-sight vector intersects the ring plane at a point which we label $(\rho_0, \phi_0, 0)$, where the *azimuthal angle* ϕ_0, is measured with respect to the x-axis. The vector $\boldsymbol{R_c}$ is the spacecraft position vector and $D = ||\boldsymbol{R_c} - \boldsymbol{\rho}||$ is the distance from the spacecraft to the point on the ring plane where the line of sight intersects. The angle B is the ring opening angle (the elevation angle of Earth above the ring plane).

Note that during the actual Cassini mission, radio waves were transmitted from the spacecraft, propagated through the rings (behaving approximately as plane waves to a high degree of accuracy), and then received at a DSN antenna on Earth. However, in the standard reconstruction method (Marouf et al. 1986), it is convenient to work with the opposite construction because this permits a straightforward Huygens-Fresnel formulation of diffraction. By reciprocity, this configuration yields identical results to the experimental configuration.

2.2. *Theory of Reconstruction*

Marouf et al. (1986) were the first to derive the equations to reconstruct the ring profiles by modeling the average effect of ring material on a ray transmitted directly through the rings using the Huygens-Fresnel principle. Consider a plane wave with frequency ω, wavelength λ, and wavenumber $k = \frac{2\pi}{\lambda}$ incident along $\hat{\boldsymbol{u}}_{\boldsymbol{i}}$ on an infinitesimally thin "gray-screen" which represents the ring plane, as in Figure 3. Then, the average complex field E_c observed at $\boldsymbol{R_c}$ can be obtained using wave optics to be approximately

$$E_0 \iint d\boldsymbol{\rho} \left[\frac{\mu_0}{i\lambda} T(\boldsymbol{\rho}) e^{ik\hat{\boldsymbol{u}}_{\boldsymbol{i}}\cdot\boldsymbol{\rho}}\right] \frac{e^{ik||\boldsymbol{R_c}-\boldsymbol{\rho}||}}{||\boldsymbol{R_c}-\boldsymbol{\rho}||} \tag{1}$$

where E_0 is a constant, $\mu_0 = \sin B$, and $T(\boldsymbol{\rho})$ is the function describing the complex transmittance of the rings.

The diffracted complex transmittance, $\hat{T}$, is defined by normalizing the observed signal. Explicitly, we have:

$$\hat{T} = \left(\frac{E_c}{E_0}\right) e^{-ik\hat{\boldsymbol{u}}_{\boldsymbol{i}}\cdot\boldsymbol{R_c}}. \tag{2}$$

Assuming that the rings have circular symmetry over the inversion range, Marouf et al. (1986) combined Eq. 1 and Eq. 2 to obtain:

$$\hat{T}(\rho_0) = \frac{\mu_0}{\lambda}\int_0^\infty \mathrm{d}\rho\ \rho T(\rho) \int_0^{2\pi} \mathrm{d}\phi \frac{e^{i\psi(\rho_0,\phi_0;\rho,\phi)}}{||\boldsymbol{R_c}-\boldsymbol{\rho}||}, \tag{3}$$

where $\boldsymbol{\rho}_0 = (\rho_0, \phi_0, 0)$ is the point of intersection between Saturn's ring plane and the line of sight from Cassini. ψ is the full *Fresnel phase*, given by:

$$\psi = k(\hat{\boldsymbol{u}}\cdot(\boldsymbol{\rho}-\boldsymbol{R}) + ||\boldsymbol{\rho}-\boldsymbol{R_c}||), \tag{4}$$

where $\hat{\boldsymbol{u}}$ is the normalized relative position vector of $\boldsymbol{R_c}$ with respect to $\boldsymbol{\rho} = (\rho, \phi)$, that is,

$$\hat{\boldsymbol{u}} = \frac{\boldsymbol{R_c}-\boldsymbol{\rho}}{||\boldsymbol{R_c}-\boldsymbol{\rho}||}. \tag{5}$$

Marouf et al. (1986) use the stationary phase approximation to simplify Eq. 3 into a one-dimensional integral equation. In rapidly oscillating integrals, the contributions to the integral come mostly from points of stationary phase, which are points where $\partial\psi/\partial\phi = 0$. If $\phi = \phi_s(\rho, \rho_0, \phi_0, B, D)$ is the solution to $\partial\psi/\partial\phi = 0$, then Eq. 3 approximately reduces to

$$\hat{T}(\rho_0) \approx \frac{1-i}{2F}\int_{-\infty}^{\infty} T(\rho) e^{i\psi(\rho_0,\phi_0;\rho,\phi_s)} \mathrm{d}\rho, \tag{6}$$

where F is the Fresnel scale, given by:

$$F^2 = \frac{\lambda D}{2}\frac{1-\cos^2 B \sin^2\phi_0}{\sin^2 B}, \tag{7}$$

and $D = ||\boldsymbol{R_c}-\boldsymbol{\rho_0}||$, which we assume to be constant.

Previously, Marouf et al. (1986) estimated ψ by iterating the Newton-Raphson method with ϕ_0 as the initial estimate to compute ϕ_s. If $\phi_{s,1}$ is the first-order Newton iterate of ϕ_s, then taking a quadratic Taylor expansion of ψ about $\phi_{s,1}$ yields:

$$\psi_Q = \frac{\pi}{2}\left(\frac{\rho-\rho_0}{F}\right)^2. \tag{8}$$

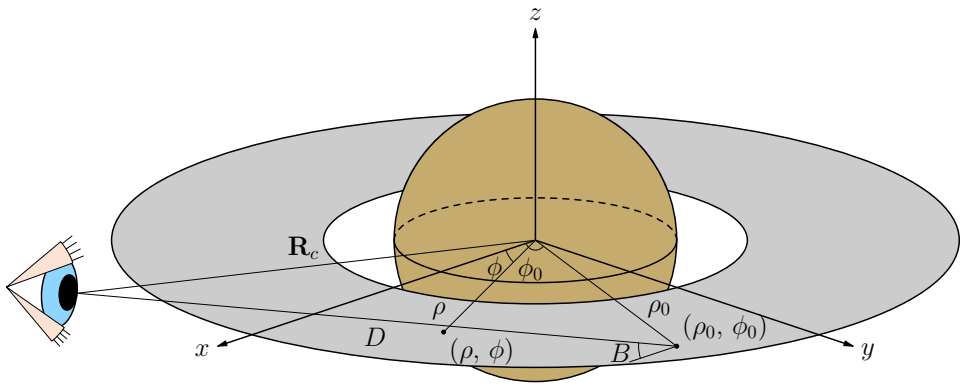

Figure 3. The geometry of an RSS occultation in a Saturnocentric coordinate system. The eye represents Cassini, and $\boldsymbol{R_c}$ is the position vector of Cassini. (ρ_0, ϕ_0) is the point where the line of sight between Cassini and receiver on Earth intersects the ring plane, and $\boldsymbol{\rho} = (\rho, \phi)$ is a dummy variable of integration.

The quadratic approximation, ψ_Q, produces the Fresnel transform:

$$\hat{T}(\rho_0) = \frac{1-i}{2F} \int_{-\infty}^{\infty} T(\rho) e^{i\frac{\pi}{2}\left(\frac{\rho-\rho_0}{F}\right)^2} \mathrm{d}\rho. \quad (9)$$

Note that Eq. 9 is a convolution-type integral. Thus, using Fourier transform techniques (Bracewell 1978), an explicit inverse can be shown to be

$$T(\rho) = \frac{1+i}{2F} \int_{-\infty}^{\infty} \hat{T}(\rho_0) e^{-i\frac{\pi}{2}\left(\frac{\rho-\rho_0}{F}\right)^2} \mathrm{d}\rho_0, \quad (10)$$

where the integral occurs over the (ρ_0, ϕ_0) plane. Note that to obtain the inverse, we took the complex conjugate of the Fresnel kernel, $\frac{1-i}{2F} e^{i\psi}$, and swapped the variable of integration. Although Eq. 6 does not have an exact mathematical inverse, we can mimic the form of Eq. 10 to obtain the following approximate inverse transform for a general ψ:

$$\tilde{T}(\rho) \approx \frac{1+i}{2F} \int_{-\infty}^{\infty} \hat{T}(\rho_0) e^{-i\psi(\rho_0,\phi_0;\rho,\phi_s)} \mathrm{d}\rho_0. \quad (11)$$

In practice the limits of integration are restricted by the available data and the desired resolution. The window width W is defined in terms of the Fresnel scale F and the resolution R via

$$W = \frac{2F^2}{R}. \quad (12)$$

Following Marouf et al. (1986), the preceding derivation assumes $\hat{\boldsymbol{u}}_{\boldsymbol{i}} \cdot \hat{\boldsymbol{u}}_{\boldsymbol{y}} = 0$, where $\hat{\boldsymbol{u}}_{\boldsymbol{y}}$ is the unit vector along the y axis. The real geometry data available from NASA's Planetary Data System (PDS) show that this dot product is small but not always zero. As the resolution becomes finer, the window width must increase, and the quadratic approximation found in Eq. 10 becomes insufficient for accurate reconstructions, and higher-order approximations of ψ are needed. However, the higher degree terms needed are more sensitive to the geometry, thus the assumption that $\hat{\boldsymbol{u}}_{\boldsymbol{i}} \cdot \hat{\boldsymbol{u}}_{\boldsymbol{y}} = 0$ becomes a source of error for large W (a few thousand kilometers or more).

To overcome this limitation, we generalized the model by eliminating the assumption that $\hat{\boldsymbol{u}}_{\boldsymbol{i}} \cdot \hat{\boldsymbol{u}}_{\boldsymbol{y}} = 0$, using the full Fresnel phase given by Eq. 4 instead of the quadratic approximation given by Eq. 8.

Moreover, instead of assuming $D = ||\boldsymbol{R_c} - \boldsymbol{\rho_0}||$ is a constant, we calculate it explicitly as a function of Cassini's location relative to Saturn.

We refer to this inversion technique as the Newton inversion method using the full geometry, which allows us to reconstruct the radial structure of the rings at up to 55m resolution.

2.3. *Optical Depth and Equivalent Depth*

The normal optical depth, which measures the opacity of the rings, can be related to the com-

plex transmittance, $T(\rho)$ by

$$\tau(\rho) = -2\mu_0 \ln(|T(\rho)|), \tag{13}$$

where $\mu_0 = \sin(B)$ and B is the ring opening angle (Marouf et al. 1986). In Figure 13 and Figure 14, we present plots of optical depth versus radial distance from Saturn that show the F ring and Strange Ringlet optical depths respectively. The equivalent depth is the radially integrated optical depth.

Noise in the observed data—additive thermal noise introduced primarily at the ground receiving station and multiplicative phase noise introduced from instability in the oscillators on the spacecraft and at the DSNs—alongside imperfections in the inversion introduce error into the calculation of the normal optical depth and equivalent depth. To limit the effect of noise in our calculations of the equivalent depth of a narrow ringlet, we model the observed ringlet opacity profile using the mathematical shape of a spectral line profile and only select occultations with high signal to noise ratio (SNR). The F ring exhibits noticeable asymmetry in many optical depth profiles (see Figure 13), so rather than using a simple Gaussian or Lorentzian, we model the curves using Ulrik Gelius' asymmetric form (Wertheim 1975).

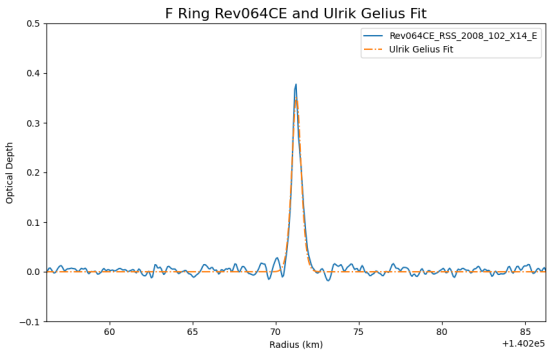

Figure 4. Optical depth profile of the F ring from Rev 064E. Reconstruction was made using the Newton inversion method at 200m and fitted with the asymmetric form due to Ulrik Gelius.

3. MIE SCATTERING THEORY

The optical depth profiles shown in Section 2.3 are especially useful in estimating particle sizes in Saturn's rings. Each band (Ka, X, and S) can only detect particles comparable in size to its wavelength or larger; as such, comparing data from all three bands allows us to roughly determine how many particles of each size exist. In particular, Mie scattering theory allows us to relate the size distribution of particles in Saturn's rings to the optical depth of the rings themselves. It has been shown that particles in Saturn's rings can be roughly modeled using a truncated power-law size distribution (Dohnanyi 1969). The number $n(a)\mathrm{d}a$ of particles per unit area with radius $a \in [a, a + \mathrm{d}a]$, $n(a)$ is given by

$$n(a) = n_0 \left(\frac{a}{a_0}\right)^{-q}, \quad a_{min} \leq a \leq a_{max}, \tag{14}$$

where n_0 is the number of particles per unit area of some arbitrary reference radius a_0 (taken to be 10cm in accordance with Jerousek et al. (2020)), q is the power-law index, and a_{min} and a_{max} are the minimum and maximum particle radii. We assume there are no particles of radius outside the interval $[a_{min}, a_{max}]$. The value of q in Saturn's rings was bounded between 2 and 4 by Dohnanyi (1969), which was improved by Brilliantov et al. (2015) to be between 2.75 and 3.5.

Furthermore, our Mie scattering model assumes that the rings are made up of several layers of discrete spherical particles distributed in accordance to the previously defined power-law. We also neglect multiple scattering effects between layers of a ring, so that light only interacts with ring material at most once. In such a model (also used in Marouf et al. (1983); Jerousek et al. (2020); Cuzzi et al. (2009)), the optical depth $\tau(\lambda)$ at a wavelength λ is given

by

$$\tau(\lambda) = \int_0^\infty \pi a^2 Q_{ext}(a,\lambda) n(a) \mathrm{d}a. \quad (15)$$

Here, we are integrating over all possible particle radii, denoted by a. Additionally, $Q_{ext}(a,\lambda)$ is the extinction (scattering plus absorption) efficiency of a particle of radius a due to radiation (light) of wavelength λ. More specifically, $Q_{ext}(a,\lambda) = \frac{\sigma_{ext}(a,\lambda)}{\pi a^2}$, where σ_{ext} is the cross section of extinction of a particle. The extinction efficiency also depends on the complex index of refraction, $\overline{m}$, which we assume to be $1.78 + 0i$ (corresponding to pure water ice) unless otherwise stated. The exact values of $Q_{ext}(a,\lambda)$ at various particle sizes for wavelengths in the Ka, X, and S bands are calculated using a Python version of the BHMIE algorithm (Bohren & Huffman 1998) and pictured in Figure 5a.

3.1. *Constraining the Size Distribution*

Though we have shown it is possible to determine the optical depth given the particle size distribution, our goal is to infer the size distribution from the opacity measurements themselves. Marouf et al. (1983) show that this can be accomplished via the differential opacity measurement $\Delta\tau(\lambda_1,\lambda_2) = \tau(\lambda_1) - \tau(\lambda_2)$. Defining $Q_\Delta(a,\lambda_1,\lambda_2) = Q_{ext}(a,\lambda_1) - Q_{ext}(a,\lambda_2)$, and given the power-law index q and a_{max}, it is possible to invert Eq. 15 to recover the following expression for $n(a_0)$:

$$\frac{\Delta\tau(\lambda_1,\lambda_2)}{\int_{a_{min}}^{a_{max}} \pi a^2 Q_\Delta(a,\lambda_1,\lambda_2) \left(\frac{a}{a_0}\right)^{-q} \mathrm{d}a}. \quad (16)$$

Given this, it only remains to determine q, a_{min}, and a_{max} in order to entirely determine the power-law size distribution of particles in Saturn's rings. Figure 5b shows that values of q and a_{max} uniquely determine normalized differential opacity $\frac{\Delta\tau(X,S)}{\tau(X)}$. The same is true for $\frac{\Delta\tau(K,X)}{\tau(K)}$; as such, we are able to significantly constrain q, a_{min}, and a_{max} by plotting $\frac{\Delta\tau(K,X)}{\tau(K)}$ and $\frac{\Delta\tau(X,S)}{\tau(X)}$ against each other as in Figure 6. Each model curve represents differential opacities across a wide range of a_{min} values and one specific combination of a_{max}, q, and $\overline{m}$. Observe that although the differential opacity is quite sensitive to changes in a_{min}, the same is not true for a_{max}: there is no significant difference between the model curves when $a_{max} = 3$m and when $a_{max} = 10$m. Thus, constraining a_{max} is better suited for near-forward occultation geometry with much smaller ring opening angles than we have. Additionally, note the small particles (around 1 millimeter) which make up the "tail" on the right side of the curves in Figure 6; as particles get to this size range, the value of a is so small compared to the wavelengths of the Ka, X, and S bands that the differential opacity remains relatively constant. As such, for each q value, these graphs saturate at some point on their tails and do not change even if a_{min} is decreased. In our results, this tends to happen when a_{min} is between 3 and 4 orders of magnitude smaller than a_{max}, and implies that decreasing a_{min} beyond 1mm would not significantly change $\frac{\Delta\tau(XS)}{\tau(X)}$ or $\frac{\Delta\tau(KX)}{\tau(X)}$. Because of this saturation, a significant portion of differential opacity values do not correspond to any power-law size distributions.

Similarly, particles much larger than the Ka, X, and S bands (around 1 meter in radius) end up at the origin of the differential opacity graph as almost no diffraction pattern is formed due to the absorption of radiation by particles much larger than its wavelength. This indicates that our results are not sensitive to particles of this size.

4. RESULTS

4.1. *The F Ring*

Due to its discontinuous nature, the F ring is only clearly detected in about a third of

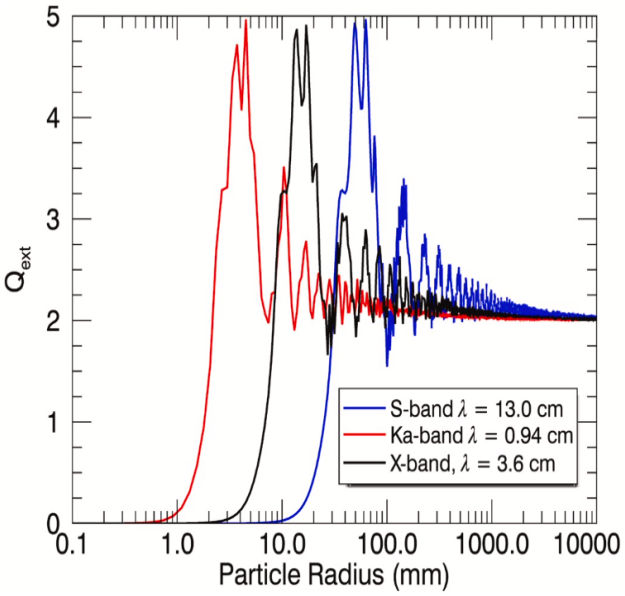

(5a) Extinction efficiency versus particle radius for the Ka band, X band, and S band, derived from Mie theory. All three curves approach 2 as particle radius increases due to Babinet's principle (Jerousek et al. 2020).

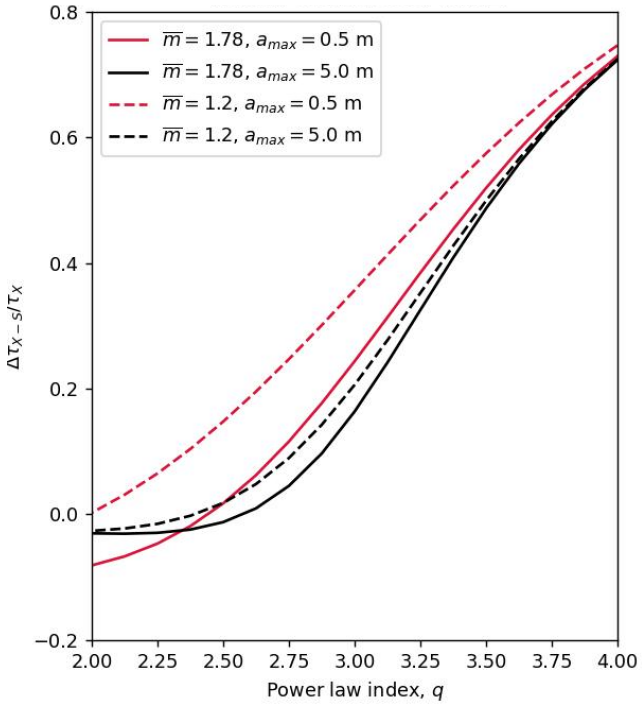

(5b) Normalized differential opacity $\frac{\Delta\tau(XS)}{\tau(X)}$ plotted against power-law index q from Marouf et al. (1983). Each curve is monotonically increasing with q and shows that a given measurement of $\frac{\Delta\tau(KX)}{\tau(X)}$ along with the value of a_{max} correspond to a unique value of q.

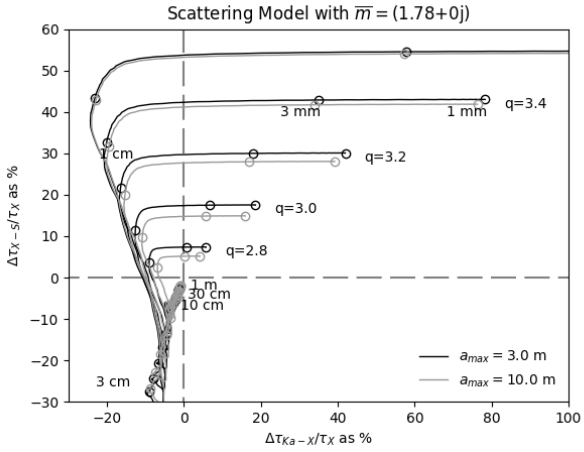

Figure 6. A differential opacity curve plotting normalized differential opacities $\frac{\Delta\tau(XS)}{\tau(X)}$ versus $\frac{\Delta\tau(KX)}{\tau(X)}$. Model curves for power-law indices from 2.8 to 3.6 in increments of 0.2 and a_{max} values of 3m and 10m are shown. For each curve, a_{min} ranges from 1mm to 1m.

Cassini occultations (Cuzzi et al. 2024). All F ring detections are identified in Appendix A. Of these occultations, we identified the few with the highest SNR, fitted them with the asymmetric form of Ulrik Gelius (see Figure 4), and integrated the profiles to find the equivalent depths. Then, we plotted the differential $\Delta\tau(KX)$ and $\Delta\tau(XS)$ opacities overlaid on several differential opacity model curves (Figure 7). We also numerically integrated the profiles directly with Simpson's Method (Burden & Faires 2011). We noticed no significant difference between the equivalent depths of the fitted profiles and the raw profiles for the F ring (see Table 2), indicating the asymmetric form due to Ulrik Gelius is an accurate fit for the F ring.

Because the differential opacity plots are extremely insensitive to the exact value of a_{max}, we assume a_{max} = 10m in accordance with Colwell et al. (2009). Calculating the resulting best fit values a_{min} and q for each occultation and averaging them yields the data in Table 1. The power law index found for the F ring (3.35 for Ulrik-Gelius fit data and 3.39 for raw data) was

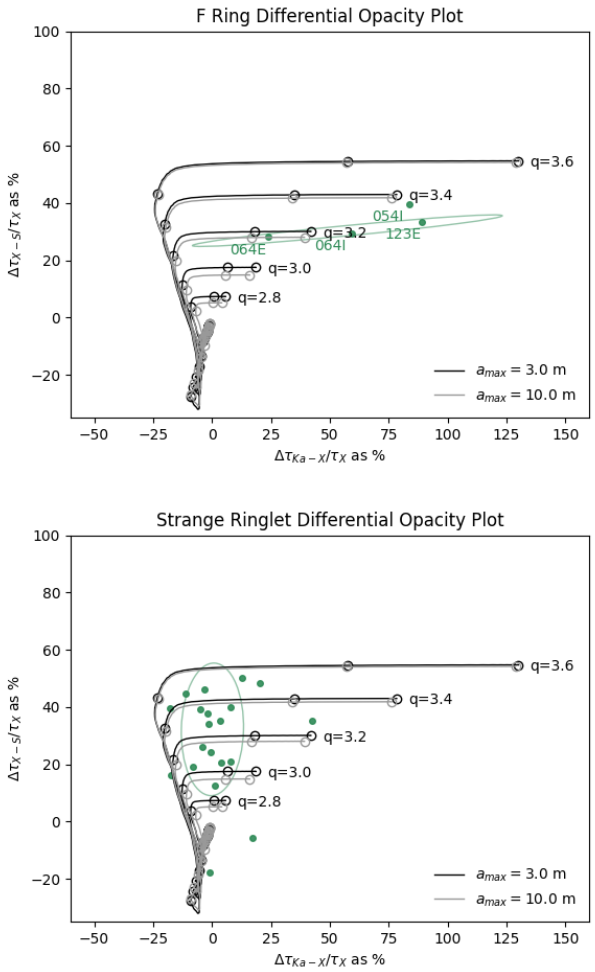

Figure 7. Normalized optical depth values plotted with model curves in the F ring and Strange ringlet. Equivalent depth values were obtained by fitting profiles to Ulrik Gelius' asymmetric form and integrating radially. The ellipse indicates a 2 standard deviation confidence interval around the mean.

significantly higher than the known values for other ring regions and the a_{min} value of 1.42mm for Ulrik-Gelius and 1.75mm for raw data was significantly lower than known values, suggesting the F ring particle size distribution contains many more small particles than other ring regions. Note that a key feature of F ring differential opacity measurements is their high normalized $\Delta\tau(KX)$ values. In particular, these values for Revs 064I, 054I, 123E, and others, are larger than the maximum possible values indicated by the model curves. Thus, the best fit power-law values for the F ring have larger error values than we see in other ring features. This indicates that particle size distributions in the F ring do not follow a standard power-law size distribution as previously assumed. We explore possible explanations to this phenomenon in Section 5.

4.2. *The Strange Ringlet*

Another narrow ringlet of interest is the Strange ringlet. Also known as R6, the Strange ringlet resides in the Huygens Gap, which separates the B ring from the Cassini Division proper (see Figure 8). The ringlet was first detected in the Voyager photo-polarimeter system (PPS) (Colwell et al. 2009) and is seen clearly in many Cassini images and occultations. It is almost opaque in some occultations and only a few kilometers wide. The Strange ringlet receives its name from its significant 7.1km average inclination with respect to the main ring plane (French et al. 2016), which causes it to sometimes appear to leave the Huygens Gap and appear superimposed in the surrounding regions. This inclination may explain its absence in Voyager occultations, which were obtained at a very low opening angle (Colwell et al. 2009).

The Strange ringlet is similar to the F ring in many ways — both are narrow, elliptical, and inclined rings and they have very similar radial widths (both the Strange ringlet and the F ring core are about 2km wide). Thus, it seems natural to compare the particle size distributions of the F ring and the Strange ringlet to determine whether the particle size distribution of the F ring is truly unique because of its chaotic environment and clumpy nature. All RSS profiles of the Strange ringlet at up to 200m resolution are shown in Appendix A.

Figure 7 compares the particle size distributions of the F ring and the Strange ringlet. Note that the size distribution of the Strange ringlet shows significantly more vertical spread than

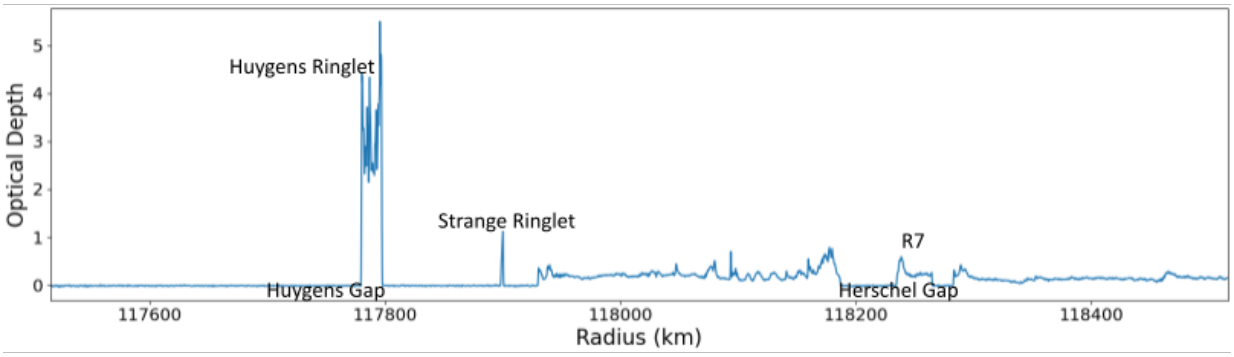

Figure 8. Occultation profile of a portion of the Cassini Division, including the Strange ringlet and its surroundings. This profile was created from the Cassini RSS Rev007 Ingress occultation, using the X43 band and Newton reconstruction method with the Fresnel phase (Eq. 11).

the F ring, but has a rather small horizontal spread with majority of the occultations showing differential KX values close to 0. This indicates that the Strange ringlet has larger particles on average than the F ring, which is supported by our calculated values of a_{min} and q (see Table 1). The Strange ringlet size distribution is closer to the calculated values of other regions, suggesting the particle size distribution in the F ring is unique.

4.3. *C Ring Plateaus*

The C ring plateaus are optically "bright" regions which wary from about 40km to about 250km in width (see Figure 1d). A total of 11 plateaus have been identified, but their origin remains unknown (Colwell et al. 2009). The optical depth at the center of each C ring plateau is several times that of the surrounding area, but the plateau's optical depths are highest in the edges, giving them a U-shaped profile (see Figure 10). Hedman & Nicholson (2014) find that the large optical depth difference between the plateaus and the C ring background are either due to differences in particle size distribution or in particle densities. We study the particle sizes within these plateaus to investigate similarities and differences within the 11 plateaus and to compare particle size distribution within the plateaus to those of narrow ringlets like the Strange ringlet and F ring.

Using the radial bounds for the plateaus identified by Colwell et al. (2009), we calculated the equivalent depth by numerically integrating the optical depth profiles within these radial bounds, then calculated the differential $\Delta\tau(KX)$ and differential $\Delta\tau(XS)$ opacities and plotted them in Fig 9. Note that the reconstructed profiles of the plateaus were much nosier for later occultations with low ring opening angles (see Fig 10). Thus, to ensure accuracy in our data, we included only occultations with a ring opening angle above 14 degrees.

Our results suggest that while the plateaus vary significantly from one another in differential $\Delta\tau(XS)$ opacity, they consistently exhibit $\Delta\tau(KX)$ values close to 0. We determined the best fit a_{min} and q values for each plateau, shown in Table 1. The noticeably large standard deviation of a_{min} for C ring plateau 11 (P11) can be attributed to its near 0 values of normalized KX and XS differential opacity, which make it difficult to exactly determine the value of a_{min} on the power law curve.

Jerousek et al. (2020) conducted a similar analysis of particle sizes on the C ring plateaus using data from stellar occultation from the Cassini UVIS and VIMS, as well as one occultation (Rev 007) from the RSS. UVIS and VIMS measured at wavelengths 0.15µm and 2.92µm respectively, meaning they detected much smaller particles than the RSS data. No-

tably, our data showed more variation among the plateaus than Jerousek et al. (2020). For example, while P6 was the plateau with the highest q mean of all plateaus in both data sets, Jerousek et al. (2020) found a q mean of 3.21 while our calculated q mean was 3.41. One possible explanation for the difference is that the RSS data is more sensitive to larger particles because it spans wavelengths of 0.94cm, 3.6cm, and 13cm, which is significantly larger than the wavelengths of UVIS and VIMS. We explore methods of consolidating our results with those of Jerousek et al. (2020) in Section 5.

Feature	n_0 Mean	n_0 SD	q Mean	q SD	a_{min} Mean (mm)	a_{min} SD (mm)
F ring (fitted)	4.60	1.31	3.35	0.10	1.42	0.73
F ring (raw)	4.03	0.90	3.39	0.14	1.75	0.72
Strange ringlet (fitted)	26.59	8.71	3.31	0.18	8.19	10.35
Strange ringlet (raw)	27.14	9.52	3.43	0.13	5.06	0.84
P1	18.57	0.56	3.18	0.10	4.08	1.08
P2	18.57	0.50	3.23	0.07	4.66	0.40
P3	18.56	0.82	3.17	0.11	4.16	0.86
P4	1.77	0.48	3.30	0.04	4.50	0.23
P5	1.84	0.73	3.02	0.05	3.74	0.55
P6	16.35	0.64	3.43	0.04	4.64	0.21
P7	18.88	0.17	3.10	0.02	4.03	0.30
P8	18.39	1.97	3.20	0.04	4.17	0.90
P9	18.86	0.30	3.21	0.03	4.21	0.24
P10	18.79	0.24	3.22	0.03	4.22	0.27
P11	13.97	6.85	2.82	0.03	65.07	241.40

Table 1. Mean and standard deviation (SD) of best fit q and a_{min} values over various ring features, along with the corresponding mean and SD of n_0. a_{max} is assumed to be 10m.

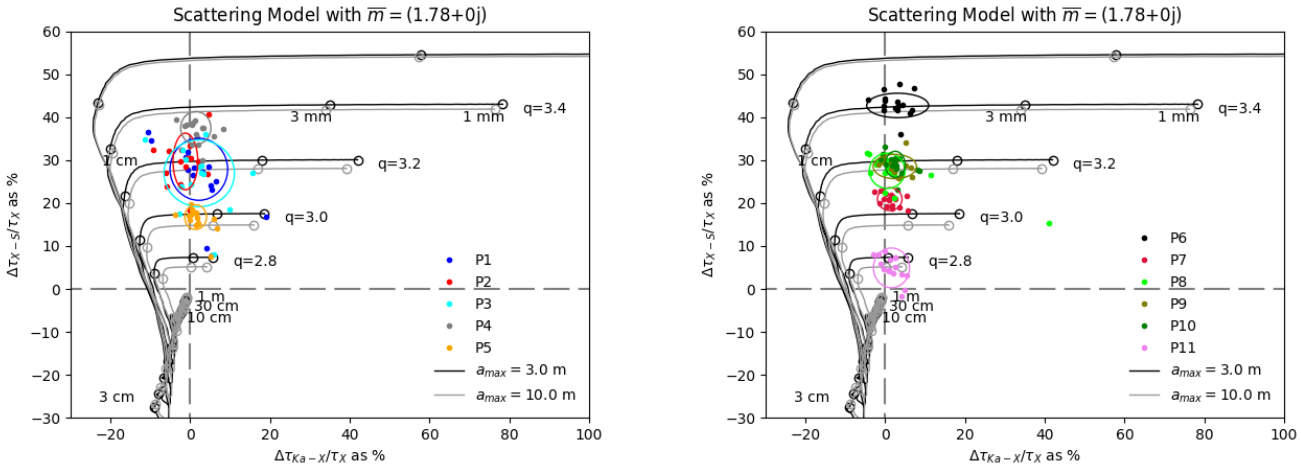

Figure 9. 2D differential opacity plot of C ring plateaus $1-5$ (left) and plateaus $6-11$ (right). Differential opacities were obtained over all RSS occultations with ring opening angle over 14 degrees. Underlaid are differential opacity curves with power laws $q = 2.8, 3.0, 3.2, 3.4$. Points $a_{min} = 0.1, 0.3, 1, 3, 10, 30$ and 100cm are identified.

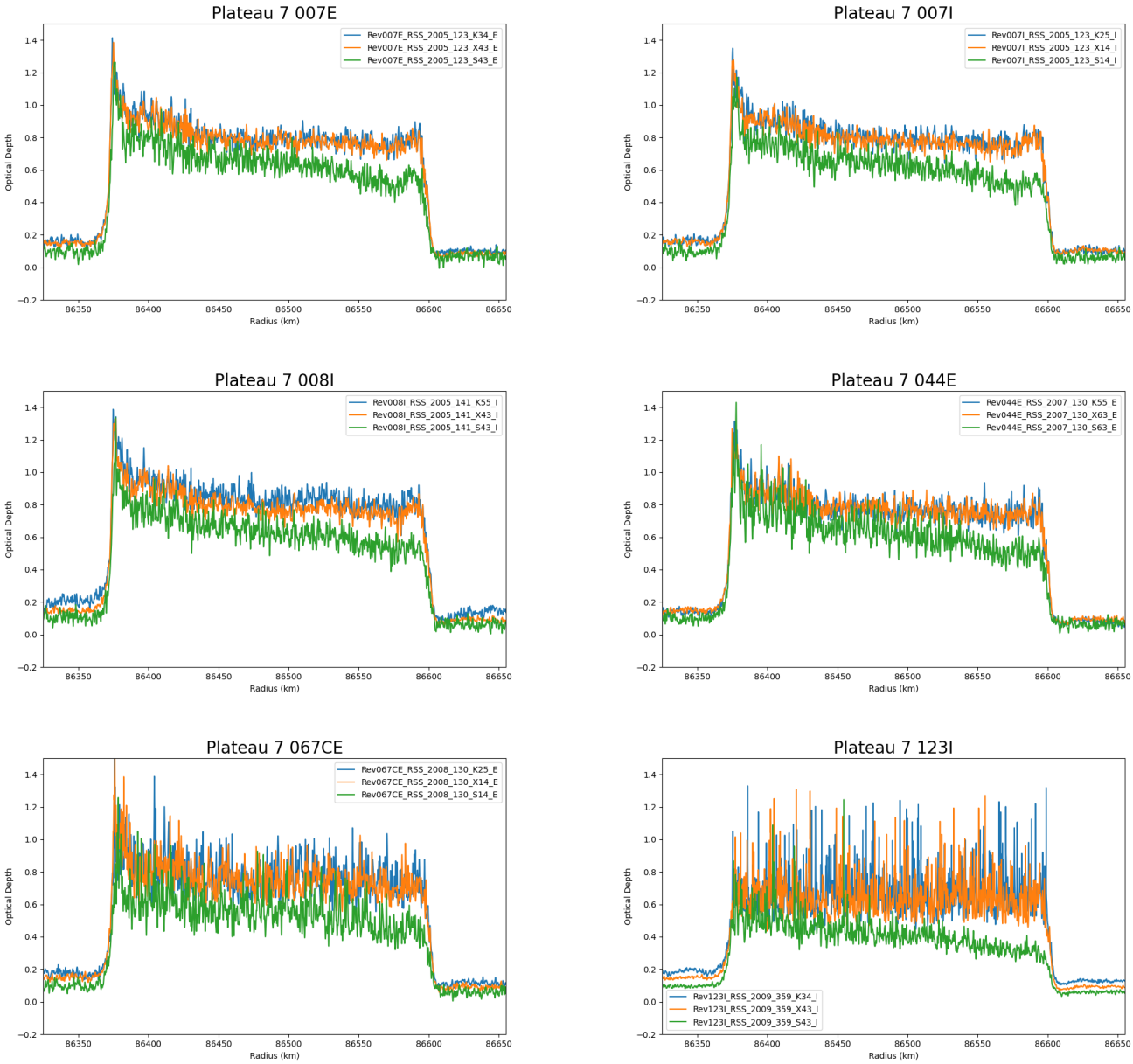

Figure 10. Optical depth profiles for Plateau 7 across a selection of occultations. Reconstructions were retrieved using the Newton inversion method at 500m resolution. Note that the SNR of the early occultations (Revs 007E, 007I, and 008I) is much higher than the SNR of the late occultations (Revs 067E and 123I).

5. DISCUSSION

Our survey of the F ring, Strange ringlet, and C ring plateaus reveals substantial regional differences in differential opacity at the Ka, X, and S radio bands. The simplest explanation for these differences is a difference in the particle size distributions between these regions. Since ring particles are icy aggregates that fragment and coalesce with interparticle collisions, the particle sizes are reflections of the dynamical environment of each region.

We assess the validity of our results by comparing our calculated best-fit power law parameters in the C ring plateaus to those of Jerousek

et al. (2020), who conducted an independent analysis of the particle size distributions in the plateaus.

Figure 11 compares the differential opacity values we obtained over all RSS occultations with sufficiently high ring opening angle with those reported by Jerousek et al. (2020), which combines optical depth measurements obtained from Cassini UVIS and VIMS with Rev007E from the RSS. Note that there appears to be some discrepancy between our differential opacities and those of Jerousek et al. (2020). However, we find close agreement between our mean differential opacity and the differential opacity values obtained from Rev007E alone. This implies that the observed discrepancy between the two calculated differential opacities arises from the inclusion of UVIS and VIMS data. Because Cassini UVIS and VIMS measure at wavelengths of a few micrometers, they are sensitive to much smaller particles than RSS data. Although our inferred particle size distributions are constrained to the regime of RSS data, sensitivity to smaller particles may still affect the resulting differential opacities.

Figure 12 presents another way to consider the difference between our results and those of Jerousek et al. (2020). The similarities between the red and blue lines demonstrate that our results are mostly in agreement with Jerousek et al. (2020) for the C ring plateaus. The largest difference occurs in P11, in which q differs by 0.24 and our value of a_{min} is roughly one order of magnitude larger. Despite this localized difference, the broad agreement in particle size parameters supports the validity of our method and its application to the various narrow ringlets analyzed in this paper.

Having established the consistency of our method with previous literature, we now consider the physical interpretation of our results for the F ring. Our analysis suggests that the F ring core consists of significantly smaller particles than Saturn's larger rings. These smaller particles may be a result of the F ring's complex dynamical environment. Since interactions with the satellite moon Prometheus perturb the F ring, they could cause more frequent collisions and result in an abundance of smaller particles. Additionally, our results provide an independent confirmation of the clumpy nature of the F ring core. Esposito et al. (2008) first detected the clumps, known as *kittens*, within the F ring using stellar occultation by UVIS and VIMS.

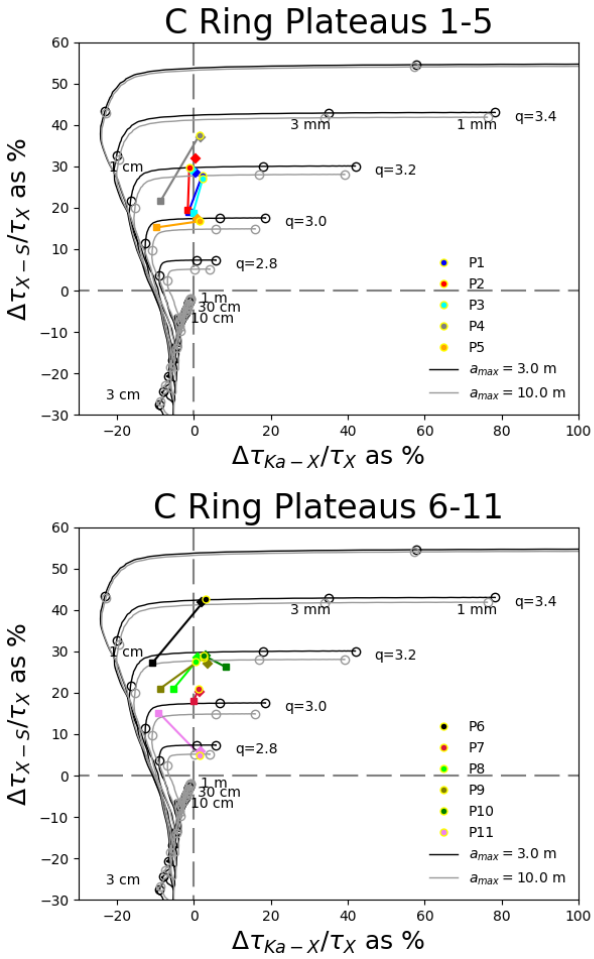

Figure 11. 2D differential opacity plot of C ring plateaus 1-5 (top) and 6-11 (bottom). Yellow-outlined dots represent the mean differential KX and XS opacity over all RSS occultation with ring opening angle over 14 degrees. Diamonds are differential opacity taken from only Rev007. Squares are values obtained from Jerousek et al. (2020).

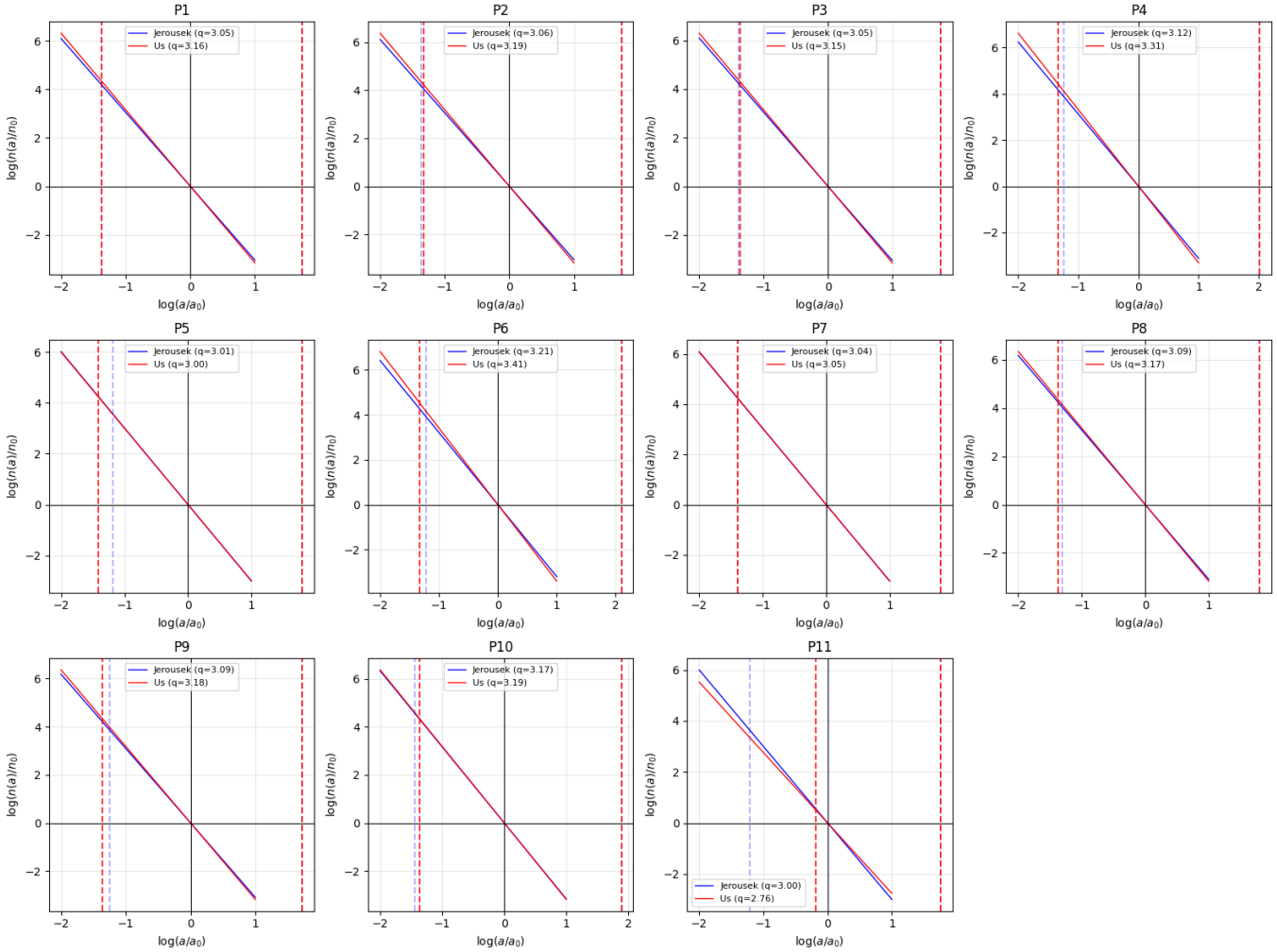

Figure 12. Plots of our observed power laws for the C ring plateaus (red) versus Jerousek's power laws (blue) with $\log(n(a)/n_0)$ on the vertical axis and $\log(a/a_0)$ on the horizontal axis. Note that both lines intersect at the origin, where $a = a_0$ and $n(a) = n(a_0)$. The slope of each line is $-q$, and the dashed vertical lines represent values of a_{min} and a_{max} over which the power laws are defined.

Alrebdi & Esposito (2025) hypothesized that only a fraction of these kittens are shepherded by Prometheus. The non-detections in approximately two thirds of RSS occultations along with the varied differential opacity across detections confirms that the F ring core is clumpy and has a differing particle size across its kittens.

Since the reconstruction method assumes radial symmetry of the rings across the processing window, the presence of kittens in the F ring may effect the accuracy of the reconstruction. An important future step would be investigating whether the purported clumpy nature of the F ring has any significant effect on the accuracy of the reconstructed optical depth profiles.

Our results also reveal quirks of the Strange ringlet. While it has much larger particles than the F ring—likely due to its position in the relatively stable Cassini Division, where less erosion and breakage of larger particles into smaller ones is likely to occur—the particle size distribution of the Strange ringlet is more similar to that of the tenuous C ring rather than the Cassini Division in which it is located. Moreover, the Strange ringlet exhibits interesting in-

ternal structures in various occultation profiles. Further steps may include investigating whether the Strange ringlet displays wave-like internal structure, which could cause the difference between its particle size distribution and that of the Cassini Division background.

Another direction for future work is to investigate particle size distributions of other ringlets and embedded ringlets within the C ring and Cassini division and compare them to our observations in the Strange ringlet and F ring. For example, some of the embedded ringlets ER1 through ER16 or the ringlets R1 through R11 may be suitable for analysis with the RSS. The approximate radial positions of these ring features are known, but since there exact radial position changes across occultations, it may also be possible to dynamically identify them for each occultation profile with a feature detection algorithm that identifies large spikes in optical depth relative to an adaptive background level.

Our analysis of similar ring features currently only considers single-scattering models of light. It may be possible to obtain better power law fits for our RSS data by using the multiple scattering model presented in Jerousek et al. (2020) along with a χ^2 minimization approach to find the single best fit model across multiple occultations in a single ring region.

SUPPLEMENTAL MATERIALS

A. RSS OCCULTATION PROFILES

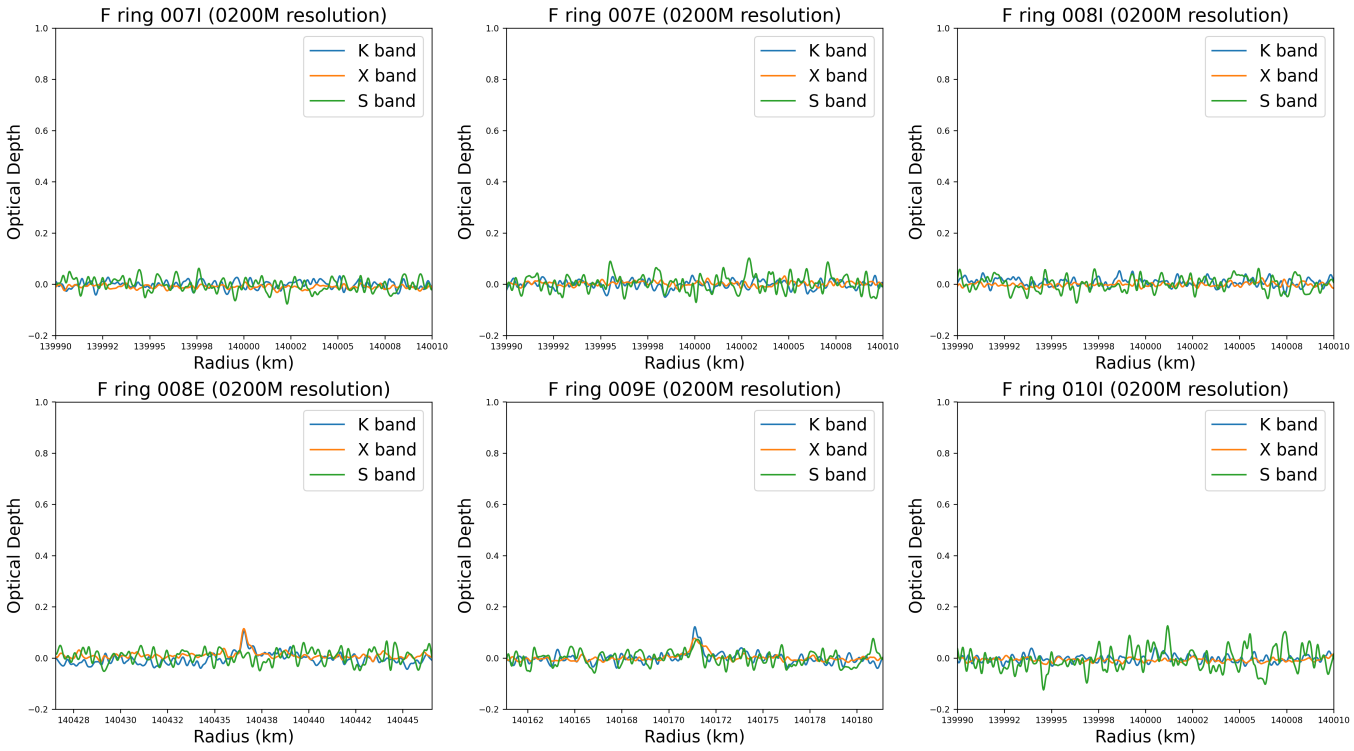

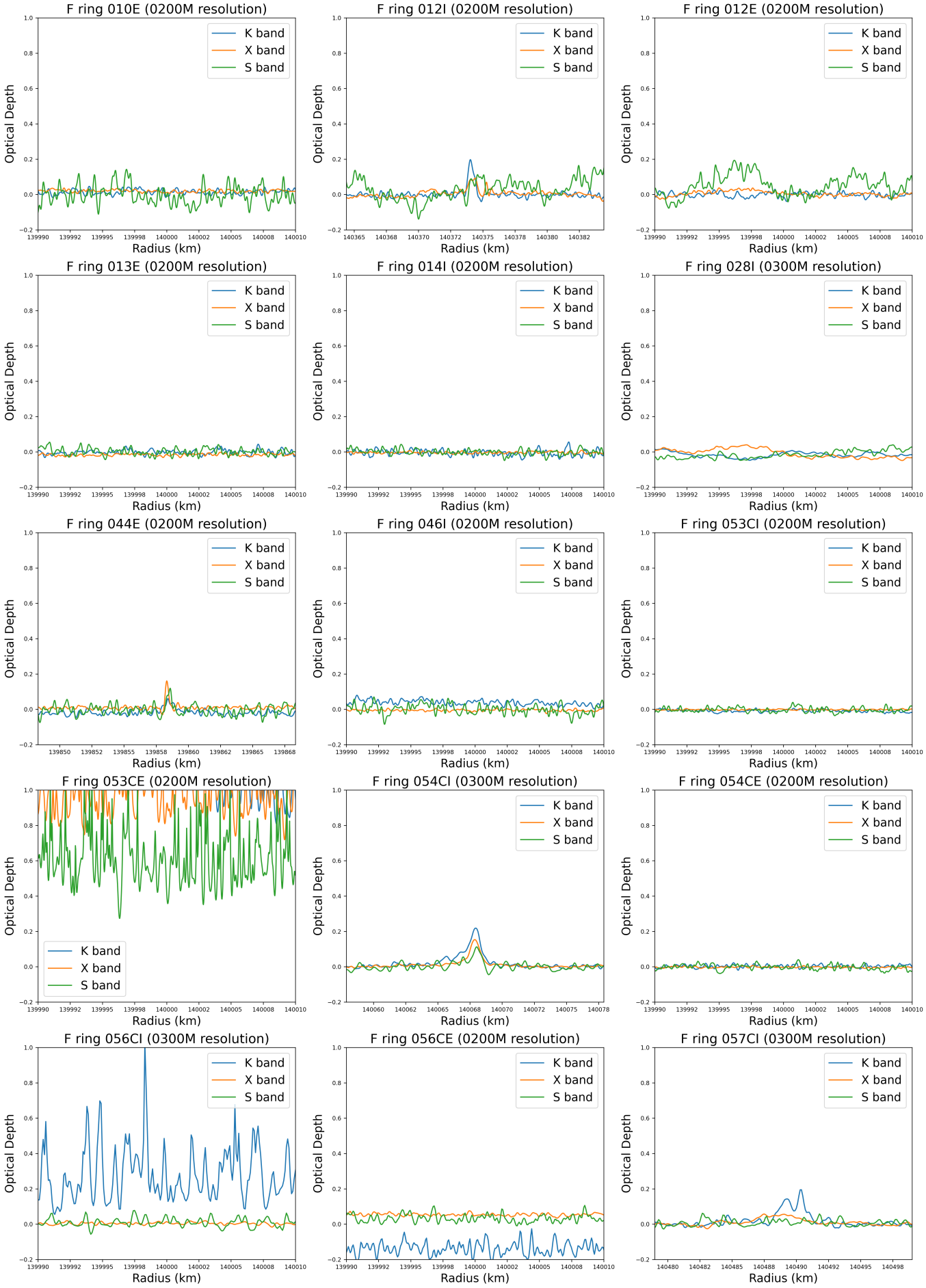
F ring 010E (0200M resolution)
F ring 012I (0200M resolution)
F ring 012E (0200M resolution)
F ring 013E (0200M resolution)
F ring 014I (0200M resolution)
F ring 028I (0300M resolution)
F ring 044E (0200M resolution)
F ring 046I (0200M resolution)
F ring 053CI (0200M resolution)
F ring 053CE (0200M resolution)
F ring 054CI (0300M resolution)
F ring 054CE (0200M resolution)
F ring 056CI (0300M resolution)
F ring 056CE (0200M resolution)
F ring 057CI (0300M resolution)
K band
X band
S band
Optical Depth
Radius (km)

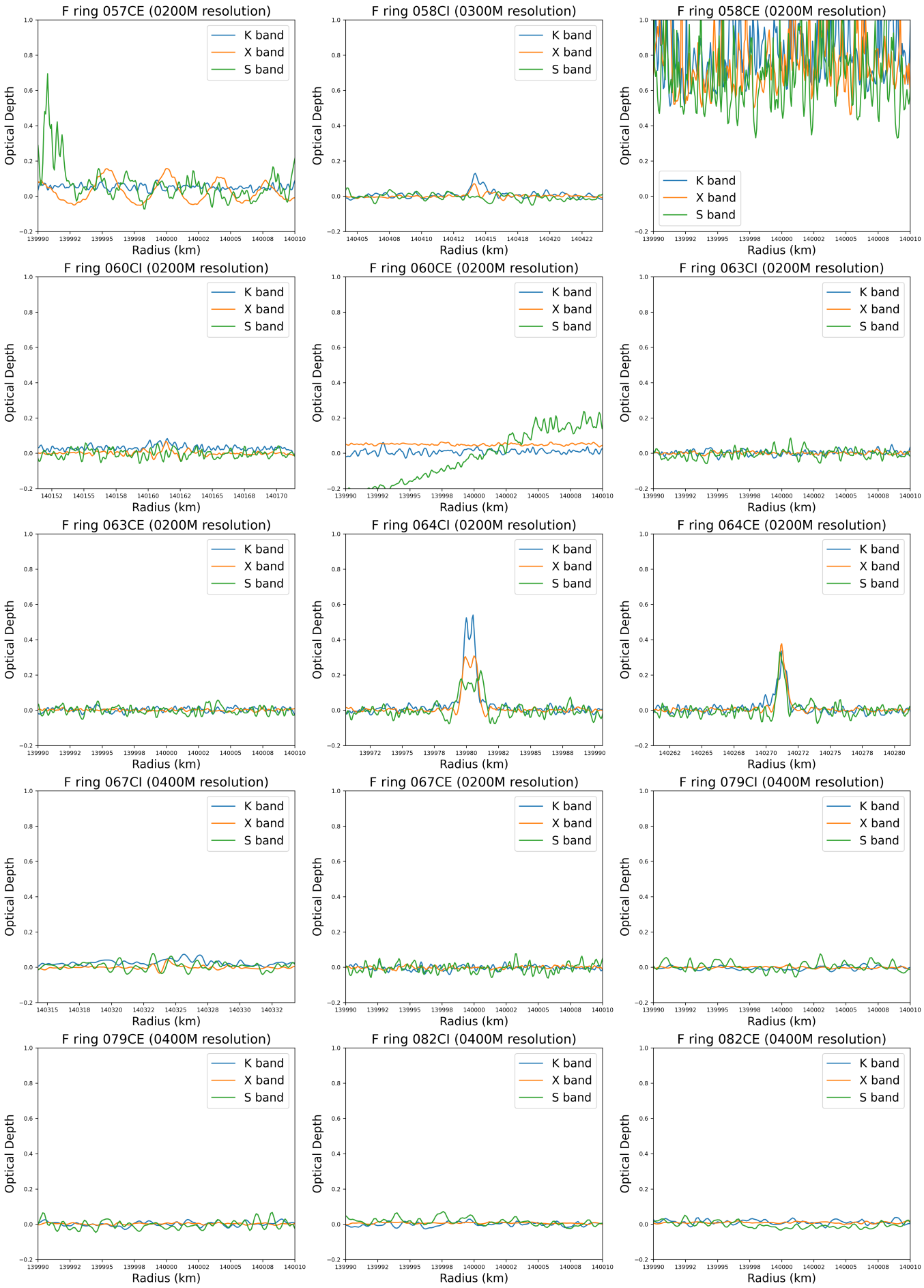
F ring 057CE (0200M resolution)
F ring 058CI (0300M resolution)
F ring 058CE (0200M resolution)
F ring 060CI (0200M resolution)
F ring 060CE (0200M resolution)
F ring 063CI (0200M resolution)
F ring 063CE (0200M resolution)
F ring 064CI (0200M resolution)
F ring 064CE (0200M resolution)
F ring 067CI (0400M resolution)
F ring 067CE (0200M resolution)
F ring 079CI (0400M resolution)
F ring 079CE (0400M resolution)
F ring 082CI (0400M resolution)
F ring 082CE (0400M resolution)
K band
X band
S band
Optical Depth
Radius (km)

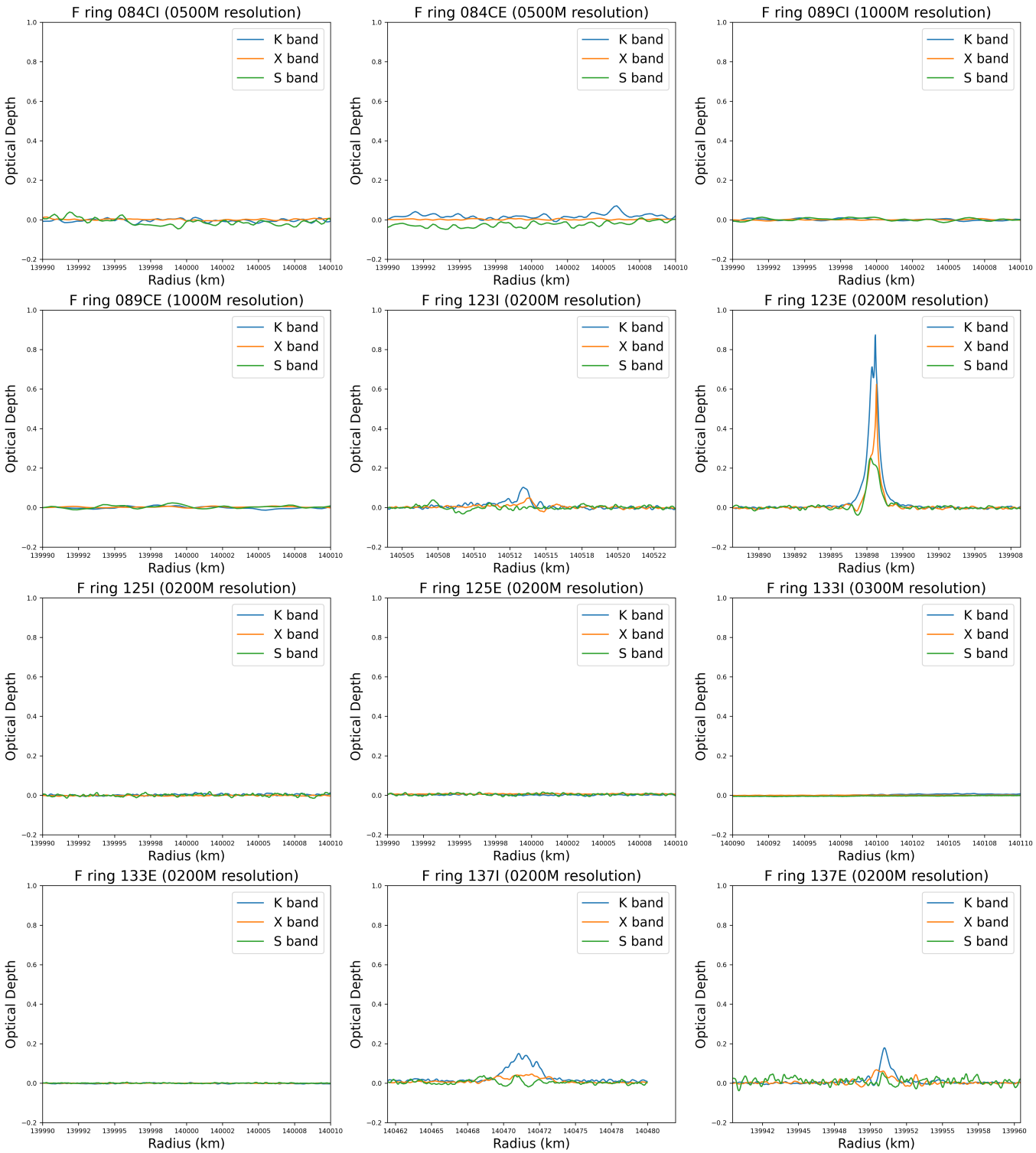

Figure 13. Gallery of normalized optical depth profiles of the F ring on three wavelengths (Ka, X, and S band) across all RSS occultations before USO failure. Revs 008E, 009E, 012I, 044E, 054I, 057I, 058I, 60I, 064I, 064E, 067I, 123I, 123E, 137I, 137E were identified as F ring detections, in line with Cuzzi et al. (2024). All other Revs are F ring non-detections. F ring detections are centered around the peak of the F ring core, while F ring non-detections are centered at $\rho = 140000$km. These profiles were obtained using the Newton inversion method. The resolution of each occultation is indicated in the figure title; majority of the occultations are at 200m resolution, except the occultations for which the geometry data was insufficient to obtain such resolution. The vertical scale (the normalized optical depth) ranges from -0.2 to 1.0.

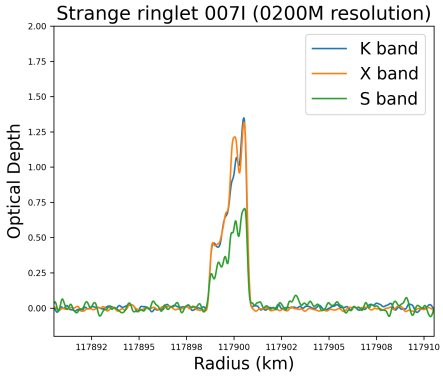
Strange ringlet 007I (0200M resolution)
K band
X band
S band
Optical Depth
Radius (km)

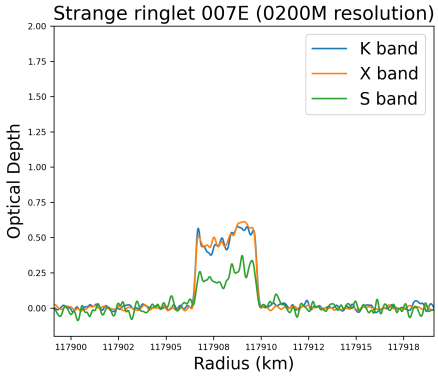
Strange ringlet 007E (0200M resolution)
K band
X band
S band
Optical Depth
Radius (km)

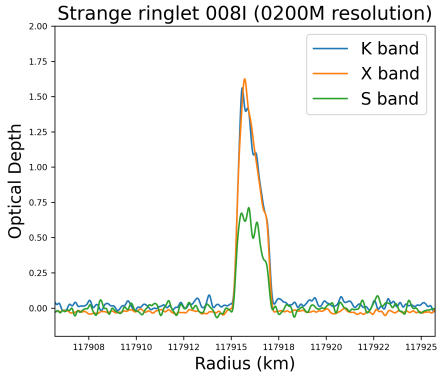
Strange ringlet 008I (0200M resolution)
K band
X band
S band
Optical Depth
Radius (km)

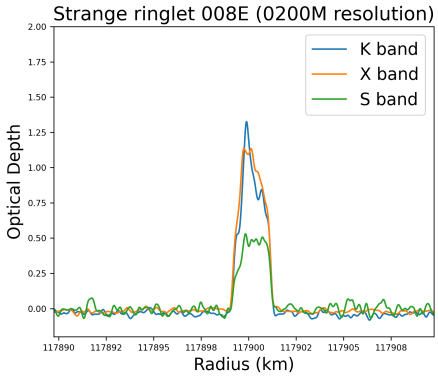
Strange ringlet 008E (0200M resolution)
K band
X band
S band
Optical Depth
Radius (km)

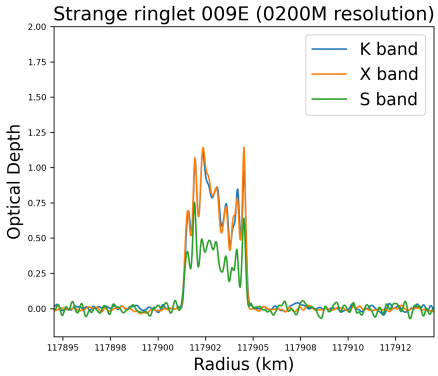
Strange ringlet 009E (0200M resolution)
K band
X band
S band
Optical Depth
Radius (km)

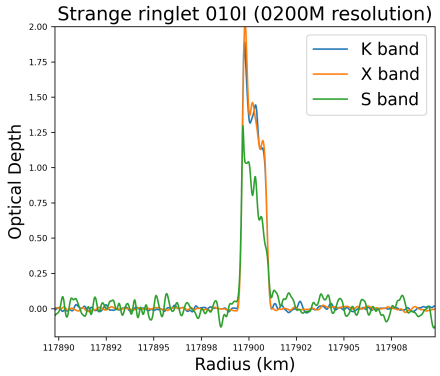
Strange ringlet 010I (0200M resolution)
K band
X band
S band
Optical Depth
Radius (km)

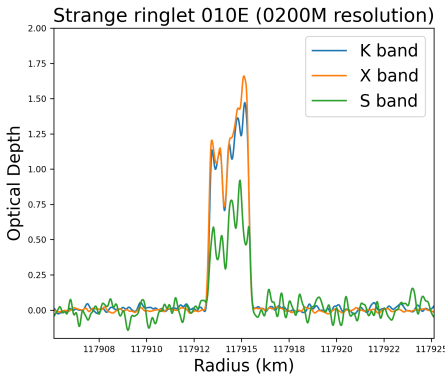
Strange ringlet 010E (0200M resolution)
K band
X band
S band
Optical Depth
Radius (km)

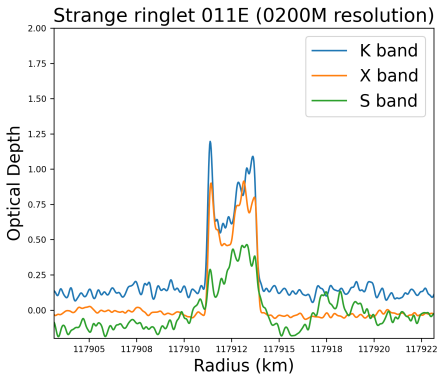
Strange ringlet 011E (0200M resolution)
K band
X band
S band
Optical Depth
Radius (km)

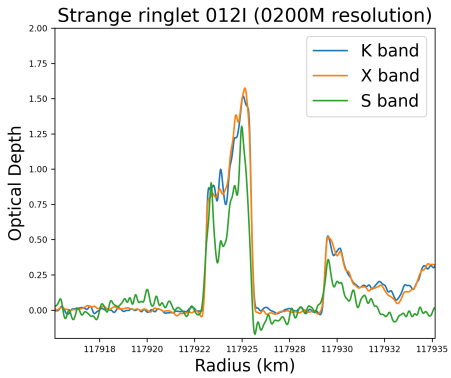
Strange ringlet 012I (0200M resolution)
K band
X band
S band
Optical Depth
Radius (km)

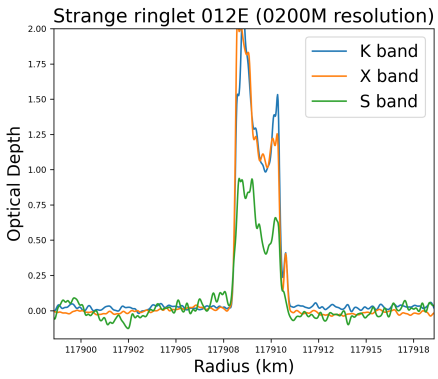
Strange ringlet 012E (0200M resolution)
K band
X band
S band
Optical Depth
Radius (km)

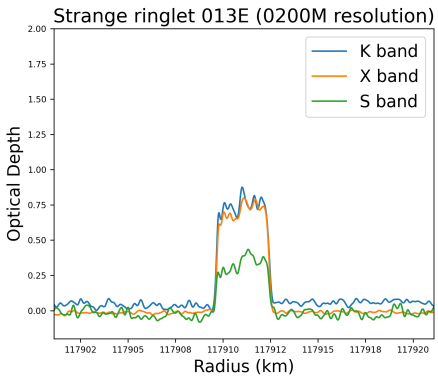
Strange ringlet 013E (0200M resolution)
K band
X band
S band
Optical Depth
Radius (km)

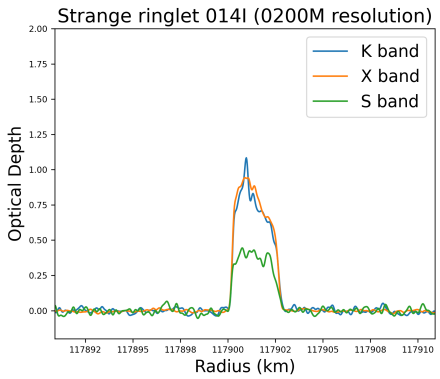
Strange ringlet 014I (0200M resolution)
K band
X band
S band
Optical Depth
Radius (km)

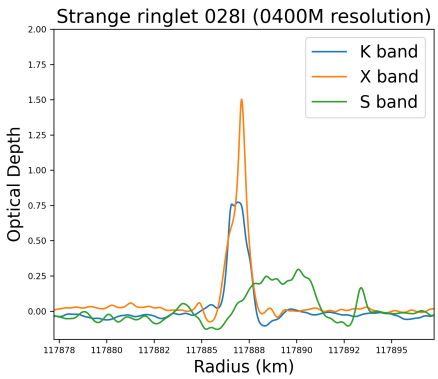
Strange ringlet 028I (0400M resolution)
K band
X band
S band
Optical Depth
Radius (km)

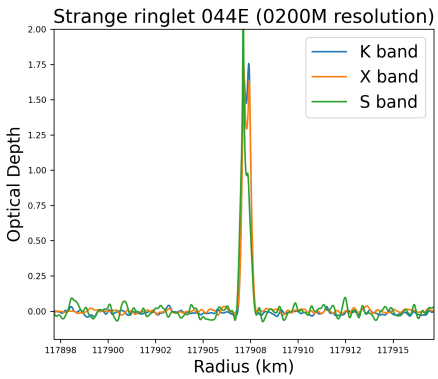
Strange ringlet 044E (0200M resolution)
K band
X band
S band
Optical Depth
Radius (km)

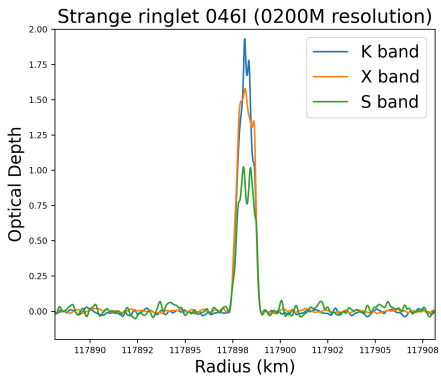
Strange ringlet 046I (0200M resolution)
K band
X band
S band
Optical Depth
Radius (km)

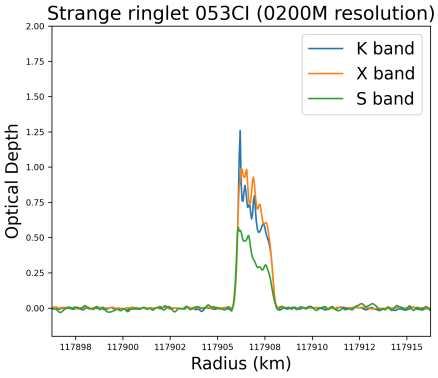
Strange ringlet 053CI (0200M resolution)
K band
X band
S band
Optical Depth
Radius (km)

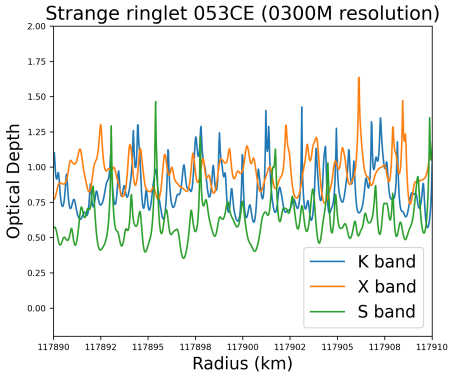
Strange ringlet 053CE (0300M resolution)
K band
X band
S band
Optical Depth
Radius (km)

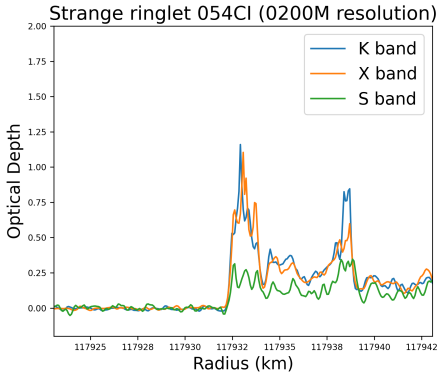
Strange ringlet 054CI (0200M resolution)
K band
X band
S band
Optical Depth
Radius (km)

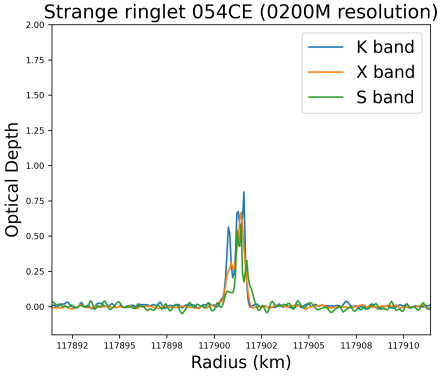
Strange ringlet 054CE (0200M resolution)
K band
X band
S band
Optical Depth
Radius (km)

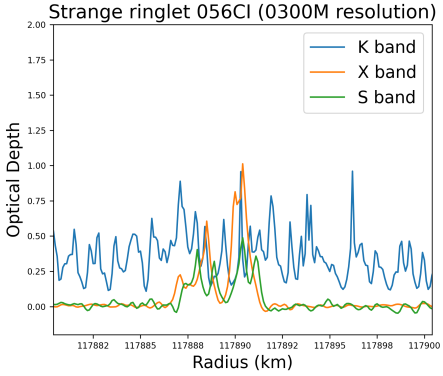
Strange ringlet 056CI (0300M resolution)
K band
X band
S band
Optical Depth
Radius (km)

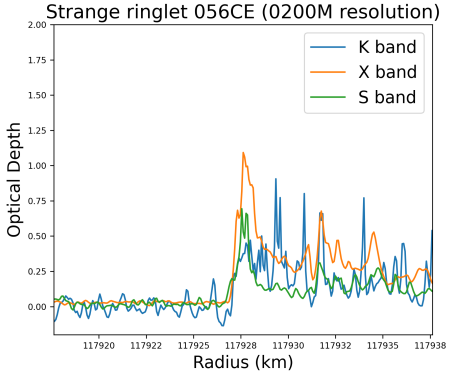
Strange ringlet 056CE (0200M resolution)
K band
X band
S band
Optical Depth
Radius (km)

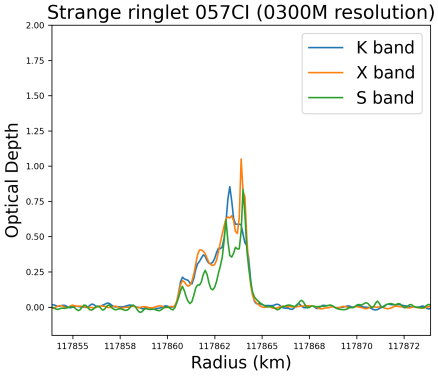
Strange ringlet 057CI (0300M resolution)
K band
X band
S band
Optical Depth
Radius (km)

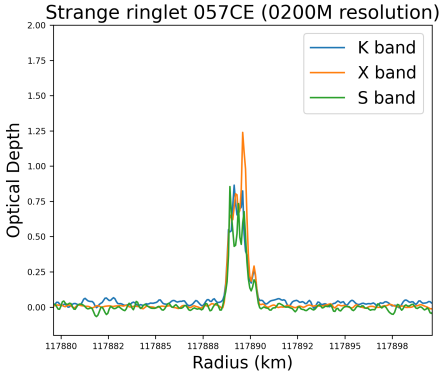
Strange ringlet 057CE (0200M resolution)
K band
X band
S band
Optical Depth
Radius (km)

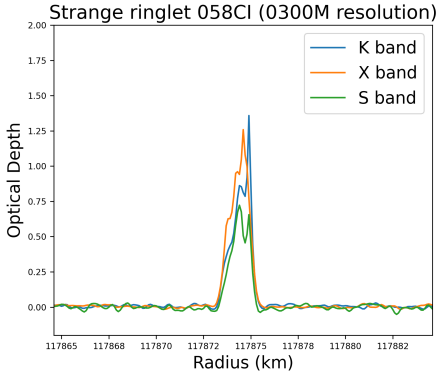
Strange ringlet 058CI (0300M resolution)
K band
X band
S band
Optical Depth
Radius (km)

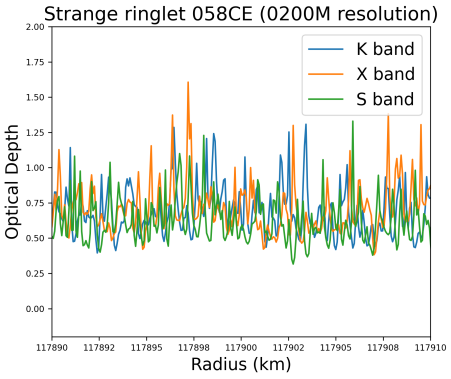
Strange ringlet 058CE (0200M resolution)
K band
X band
S band
Optical Depth
Radius (km)

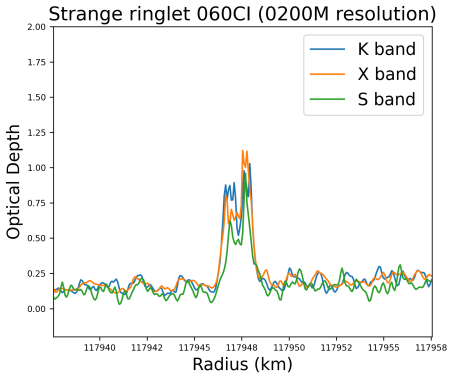
Strange ringlet 060CI (0200M resolution)
K band
X band
S band
Optical Depth
Radius (km)

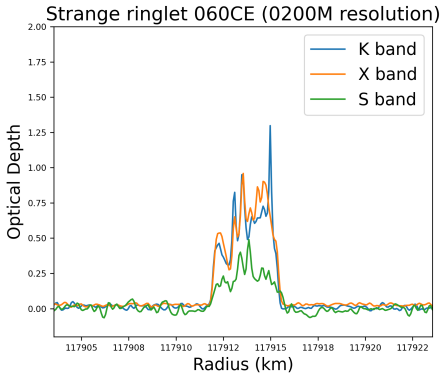
Strange ringlet 060CE (0200M resolution)
K band
X band
S band
Optical Depth
Radius (km)

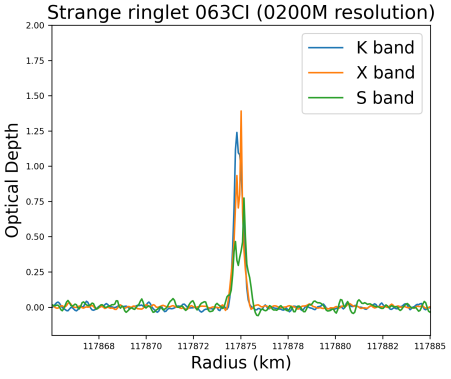
Strange ringlet 063CI (0200M resolution)
K band
X band
S band
Optical Depth
Radius (km)

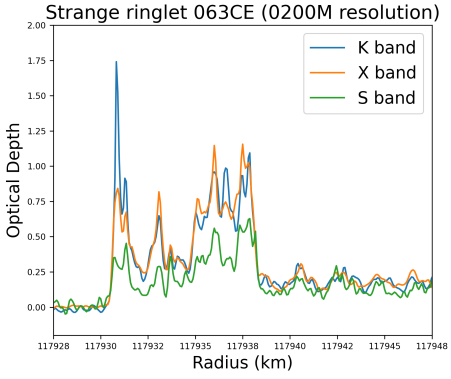
Strange ringlet 063CE (0200M resolution)
K band
X band
S band
Optical Depth
Radius (km)

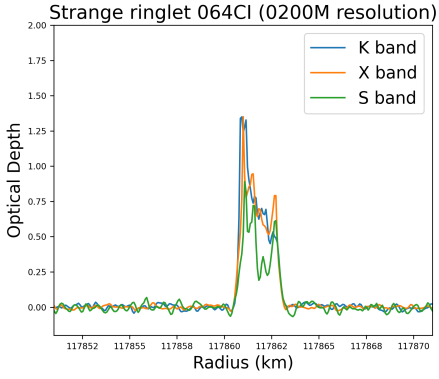
Strange ringlet 064CI (0200M resolution)
K band
X band
S band
Optical Depth
Radius (km)

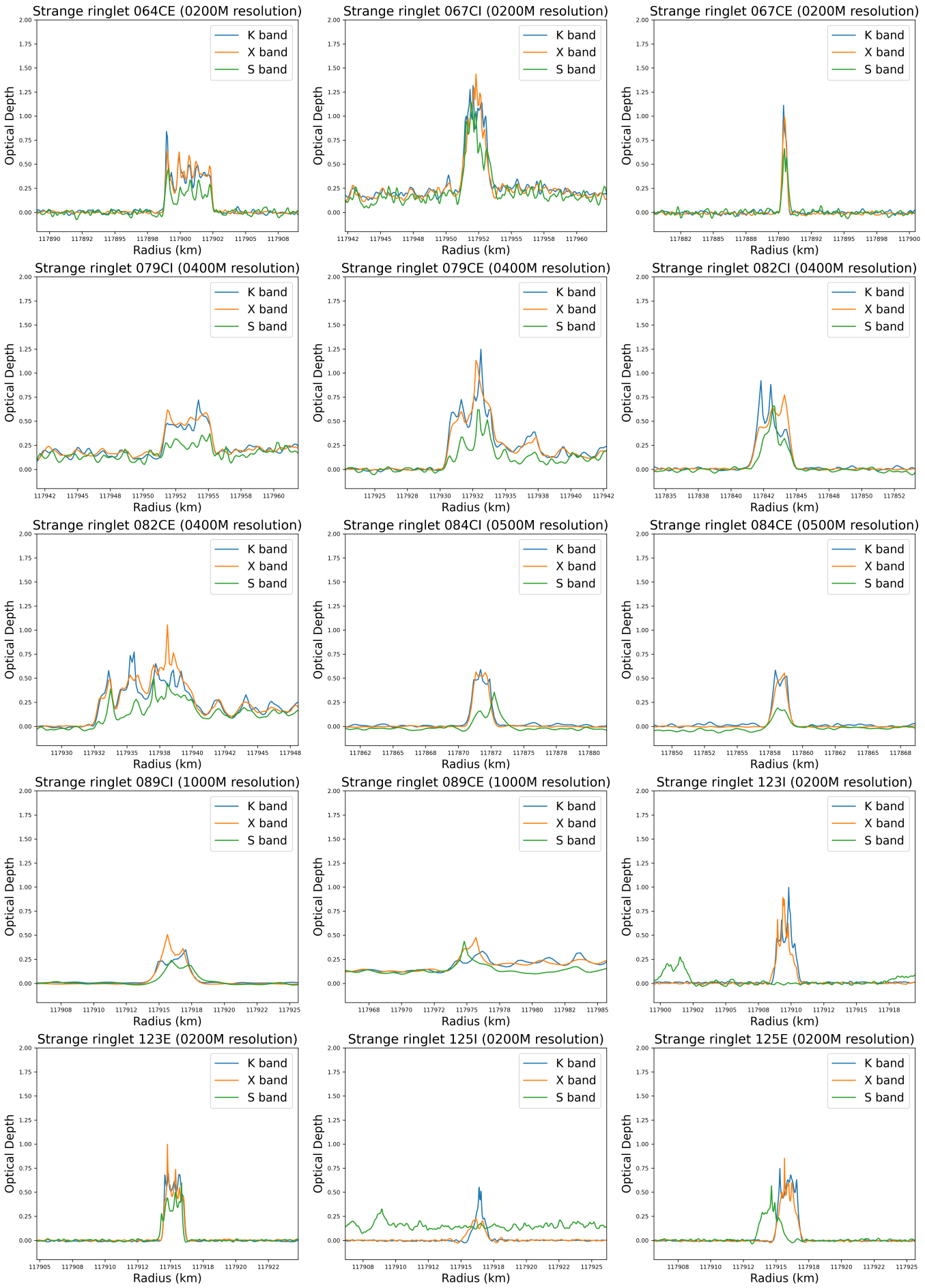
Strange ringlet 064CE (0200M resolution)
Strange ringlet 067CI (0200M resolution)
Strange ringlet 067CE (0200M resolution)
Strange ringlet 079CI (0400M resolution)
Strange ringlet 079CE (0400M resolution)
Strange ringlet 082CI (0400M resolution)
Strange ringlet 082CE (0400M resolution)
Strange ringlet 084CI (0500M resolution)
Strange ringlet 084CE (0500M resolution)
Strange ringlet 089CI (1000M resolution)
Strange ringlet 089CE (1000M resolution)
Strange ringlet 123I (0200M resolution)
Strange ringlet 123E (0200M resolution)
Strange ringlet 125I (0200M resolution)
Strange ringlet 125E (0200M resolution)
K band
X band
S band
Optical Depth
Radius (km)

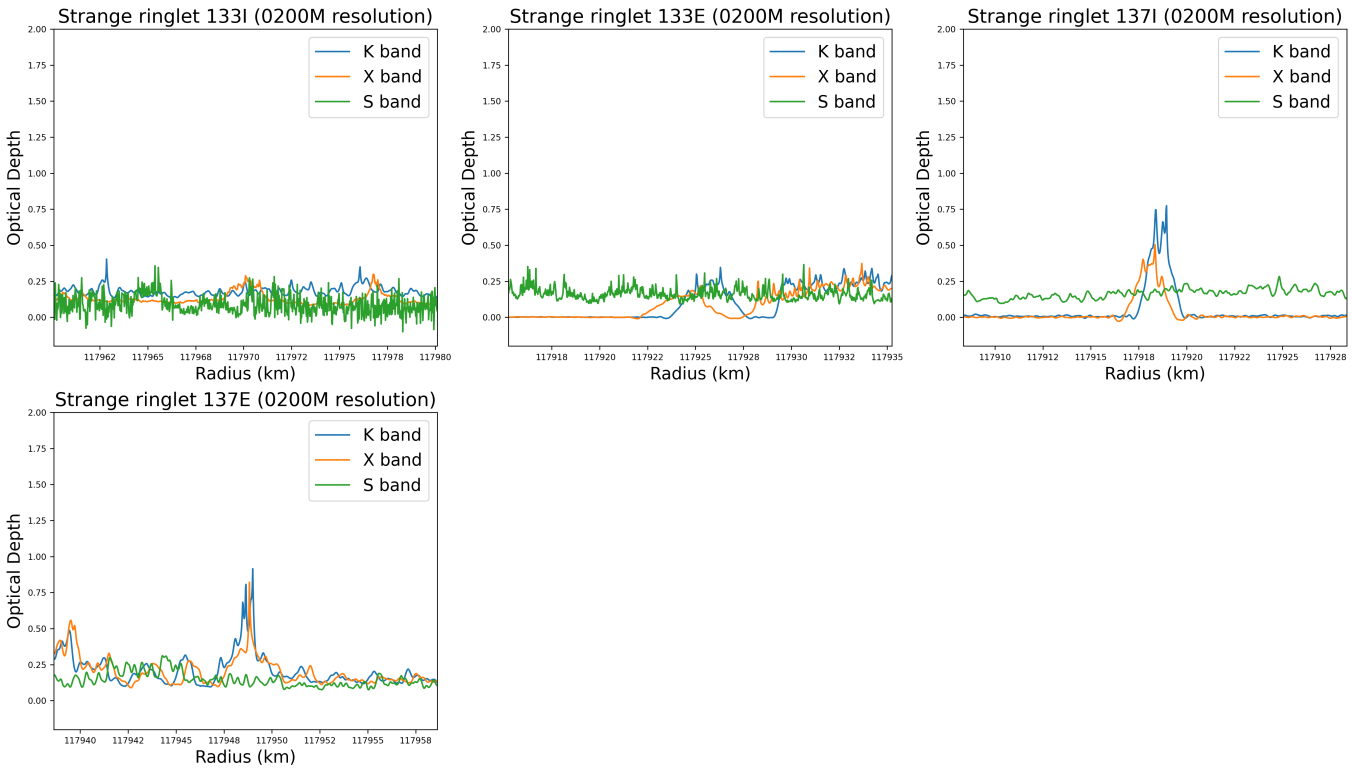

Figure 14. Gallery of normalized optical depth profiles of the Strange ringlet on three wavelengths (Ka, X, and S band) across a representative selection of occultations. These profiles were obtained using the Newton inversion method, and are all at 200m resolution. The vertical scale (the normalized optical depth) ranges from −0.2 to 2.25.

B. RSS OCCULTATION DATA

Table 2. Cassini RSS ring occultation times, geometries, depths, and widths of F ring: Of the 23 Cassini RSS detections of the F ring, we identified the 4 with clear detections and high SNR across all three bands. This table lists the center-crossing time, radial distance from the center of Saturn to the ringlet center, and ring opening angle (also known as B angle) for each revolution. It also lists the full-width at half maximum (FWHM) and the calculated equivalent depth (Fit EQD) of the fitted Ulrik Gelius profile model, along with the numerically integrated equivalent depth of the unfitted profile (Raw EDQD).

Rev	Band	Date and Time (UTC)	Res (m)	Radius (km)	B angle (deg)	Fit FWHM (km)	Fit EQD (km)	Raw EQD (km)
054I	K	2007-12-19T02:29:39.2757	200	140067.76741	-6.62257	1.20555	0.32666	0.37069
054I	X	2007-12-19T02:29:39.2750	200	140067.80539	-6.62257	0.83190	0.17767	0.21404
054I	S	2007-12-19T02:29:39.2862	200	140067.18241	-6.62257	0.79591	0.10710	0.11291
064I	K	2008-04-11T06:42:21.9389	200	139980.21408	-9.78316	0.72864	0.65258	0.63808

Rev	Band	Date and Time (UTC)	Res (m)	Radius (km)	B angle (deg)	Fit FWHM (km)	Fit EQD (km)	Raw EQD (km)
064I	X	2008-04-11T06:42:21.9385	200	139980.24063	-9.78316	0.91148	0.40930	0.38517
064I	S	2008-04-11T06:42:22.0531	200	139980.40322	-9.78316	0.96736	0.28866	0.28521
064E	K	2008-04-11T06:42:17.6159	200	140271.20764	-9.78316	0.82760	0.35638	0.32631
064E	X	2008-04-11T06:42:17.6143	200	140271.31933	-9.78316	0.55516	0.28832	0.26914
064E	S	2008-04-11T06:42:17.7297	200	140271.43612	-9.78316	0.53151	0.20718	0.19580
123E	K	2009-12-26T03:26:47.1310	200	139897.97416	4.83006	0.60122	0.67300	0.75016
123E	X	2009-12-26T03:26:47.1442	200	139898.06626	4.83006	0.57686	0.35563	0.34400
123E	S	2009-12-26T03:26:47.1436	200	139898.06167	4.83006	0.47782	0.23669	0.23670

Table 3. **Cassini RSS ring occultation times, geometries, depths, and widths of Strange Ringlet:** We selected 17 RSS occultations with the highest SNR detections of the Strange Ringlet. This table lists the center-crossing time, radial distance from the center of Saturn to the ringlet center, and ring opening angle (also known as B angle) for each revolution. It also lists the full-width at half maximum (Fit FWHM) and the calculated equivalent depth (Fit EQD) of the fitted Ulrik Gelius profile model, along with the numerically integrated equivalent depth of the unfitted profile (Raw EQD).

Rev	Band	Date and Time (UTC)	Res (m)	Radius (km)	B angle (deg)	Fit FWHM (km)	Fit EQD (km)	Raw EQD (km)
007I	K	2005-05-03T03:26:41.6830	200	117900.07531	-23.57341	0.96640	1.58324	1.58496
007I	X	2005-05-03T03:26:41.6848	200	117900.05232	-23.57341	0.95776	1.63448	1.62401
007I	S	2005-05-03T03:26:41.5821	200	117900.07911	-23.57341	1.04621	0.93427	0.94094
008I	K	2005-05-21T07:51:46.2809	200	117915.97271	-23.17006	0.92390	2.00002	2.04426
008I	X	2005-05-21T07:51:46.2821	200	117915.95820	-23.17006	0.85677	1.95345	1.81532
008I	S	2005-05-21T07:51:46.2799	200	117915.98521	-23.17006	0.91158	0.96393	0.87416
008E	K	2005-05-21T12:39:18.1854	200	117900.15049	-23.17006	0.96514	1.66317	1.48640
008E	X	2005-05-21T12:39:18.1858	200	117900.15568	-23.17006	1.01712	1.84121	1.72141
008E	S	2005-05-21T12:39:18.1956	200	117900.28458	-23.17006	1.05005	0.87869	0.81783
010I	K	2005-06-26T17:51:50.6829	200	117900.20396	-22.00900	0.80574	1.96484	1.87275
010I	X	2005-06-26T17:51:50.6838	200	117900.19381	-22.00900	0.79400	2.00085	1.88684
010I	S	2005-06-26T17:51:50.6885	200	117900.13564	-22.00900	0.81522	1.27845	1.26218
010E	K	2005-06-26T22:49:4.1061	200	117914.47740	-22.00900	1.30799	2.61153	2.49419
010E	X	2005-06-26T22:49:4.1078	200	117914.49788	-22.00900	1.30405	2.79042	2.65108
010E	S	2005-06-26T22:49:4.1096	200	117914.52098	-22.00900	1.22870	1.30868	1.29853
012E	K	2005-08-02T13:31:2.1434	200	117909.13582	-20.53284	1.52300	3.69254	3.55617
012E	X	2005-08-02T13:31:2.1303	200	117908.97018	-20.53284	1.36637	3.60203	3.21817
012E	S	2005-08-02T13:31:2.2837	200	117908.97066	-20.53284	1.54012	2.17449	2.01822
013E	K	2005-08-20T19:15:1.4193	200	117911.08962	-19.76151	1.72116	2.28276	2.22268

Rev	Band	Date and Time (UTC)	Res (m)	Radius (km)	B angle (deg)	Fit FWHM (km)	Fit EQD (km)	Raw EQD (km)
013E	X	2005-08-20T19:15:1.4208	200	117911.10765	-19.76151	1.59420	2.04876	1.92246
013E	S	2005-08-20T19:15:1.4271	200	117911.18549	-19.76151	1.49039	0.94748	0.85063
014I	K	2005-09-05T13:29:19.8841	200	117901.29174	-19.12301	1.33535	1.88438	1.80655
014I	X	2005-09-05T13:29:19.8837	200	117901.29577	-19.12301	1.33906	1.97922	1.88982
014I	S	2005-09-05T13:29:19.8780	200	117901.35515	-19.12301	1.39194	0.96098	0.88556
053I	K	2007-12-03T05:30:5.7885	200	117906.77923	-6.67882	1.07680	1.34312	1.27188
053I	X	2007-12-03T05:30:5.7869	200	117906.81378	-6.67882	1.04530	1.49855	1.43572
053I	S	2007-12-03T05:30:5.7931	200	117906.67715	-6.67882	1.04587	0.76667	0.74831
057I	K	2008-01-27T18:25:54.9514	300	117863.18182	-7.37773	1.64827	1.55254	1.55815
057I	X	2008-01-27T18:25:54.9513	300	117863.18881	-7.37773	1.75019	1.63308	1.61508
057I	S	2008-01-27T18:25:54.9475	300	117863.48834	-7.37773	1.39465	1.04293	1.08757
057E	K	2008-01-27T18:25:54.6122	200	117889.33480	-7.37773	0.72073	0.83604	0.96374
057E	X	2008-01-27T18:25:54.6107	200	117889.45109	-7.37773	0.71194	1.00528	0.99804
057E	S	2008-01-27T18:25:54.6121	200	117889.34343	-7.37773	0.73391	0.69342	0.67258
058I	K	2008-02-08T17:00:52.4817	300	117874.56147	-7.79319	0.81782	1.17326	1.20324
058I	X	2008-02-08T17:00:52.4835	300	117874.42607	-7.79319	0.84000	1.39304	1.36612
058I	S	2008-02-08T17:00:52.4833	300	117874.43818	-7.79319	0.78275	0.78973	0.72107
064I	K	2008-04-11T06:48:1.1365	200	117861.39948	-9.78316	1.06054	1.55564	1.70885
064I	X	2008-04-11T06:48:1.1318	200	117861.69535	-9.78316	1.33551	1.52107	1.59036
064I	S	2008-04-11T06:48:1.2355	200	117861.66361	-9.78316	1.32136	1.05270	1.01281
082I	K	2008-08-26T14:02:3.2884	400	117842.91699	-5.59271	1.52503	0.00000	1.47891
082I	X	2008-08-26T14:02:3.2841	400	117843.38955	-5.59271	1.60026	1.60926	1.54662
082I	S	2008-08-26T14:02:3.2855	400	117843.23632	-5.59271	1.20058	0.93628	0.91648
084E	K	2008-09-10T07:55:29.1293	500	117858.31325	-4.73693	0.84401	0.00000	0.70200
084E	X	2008-09-10T07:55:29.1290	500	117858.35305	-4.73693	0.74394	0.00000	0.59266
084E	S	2008-09-10T07:55:29.1293	500	117858.31118	-4.73693	0.79483	0.00000	0.13488
089I	K	2008-10-17T02:47:38.8455	1000	117916.14350	-2.73767	1.39701	0.75387	0.73015
089I	X	2008-10-17T02:47:38.8463	1000	117916.02179	-2.73767	1.50524	0.91970	0.86283
089I	S	2008-10-17T02:47:38.8429	1000	117916.54013	-2.73767	1.76165	0.55174	0.50614
123E	K	2009-12-26T02:39:47.1122	200	117915.25862	4.83006	0.95540	0.97350	0.88939
123E	X	2009-12-26T02:39:47.1091	200	117915.23271	4.83006	0.93967	0.89941	0.85051
123E	S	2009-12-26T02:39:47.1040	200	117915.18925	4.83006	1.00465	0.65324	0.61805

ACKNOWLEDGMENTS

We would like to thank our mentors Professor Richard French and Dr. Ryan Maguire for proposing this project, providing background knowledge, suggesting ideas, and helping edit this paper. Without their invaluable guidance, support, and expertise, this project would have been impossible. We are also grateful to the MIT PRIMES-USA program for providing this research opportunity. Finally, we would like to thank Professor Matt Hedman, Professor Phil Nicholson, and Dr. Richard Jerousek for offering helpful insights during discussions of this work.

REFERENCES

Alrebdi, A., & Esposito, L. W. 2025, Icarus, 441, 116709, doi: https://doi.org/10.1016/j.icarus.2025.116709

Asmar, S. W., French, R. G., Marouf, E. A., et al. 2018, Cassini Radio Science User's Guide, 1st edn., NASA Jet Propulsion Laboratory

Bohren, C. F., & Huffman, D. R. 1998, Absorption and Scattering of Light by Small Particles (New York: Wiley), 530

Bosh, A., Olkin, C., French, R., & Nicholson, P. 2002, Icarus, 157, 57, doi: https://doi.org/10.1006/icar.2002.6791

Bracewell, R. N. 1978, The Fourier Transform and Its Applications (New York: McGraw–Hill)

Brilliantov, N., Krapivsky, P. L., Bodrova, A., et al. 2015, Proceedings of the National Academy of Sciences, 112, 9536, doi: 10.1073/pnas.1503957112

Burden, R. L., & Faires, J. D. 2011, Numerical Analysis, 9th edn. (Cengage Learning)

Colwell, J. E., Nicholson, P. D., Tiscareno, M. S., et al. 2009, The Structure of Saturn's Rings, ed. M. K. Dougherty, L. W. Esposito, & S. M. Krimigis (Dordrecht: Springer Netherlands), 375–412, doi: 10.1007/978-1-4020-9217-6_13

Cuzzi, J., Clark, R., Filacchione, G., et al. 2009, in Saturn from Cassini-Huygens, ed. M. K. Dougherty, L. W. Esposito, & S. M. Krimigis (Dordrecht: Springer Netherlands), 459–509, doi: 10.1007/978-1-4020-9217-6_15

Cuzzi, J. N., Marouf, E. A., French, R. G., Murray, C. D., & Cooper, N. J. 2024, Science Advances, 10, eadl6601, doi: 10.1126/sciadv.adl6601

Dohnanyi, J. S. 1969, Journal of Geophysical Research (1896-1977), 74, 2531, doi: https://doi.org/10.1029/JB074i010p02531

Esposito, L. W., Meinke, B. K., Colwell, J. E., Nicholson, P. D., & Hedman, M. M. 2008, Icarus, 194, 278, doi: https://doi.org/10.1016/j.icarus.2007.10.001

French, R. G., Nicholson, P. D., McGhee-French, C. A., et al. 2016, Icarus, 274, 131, doi: https://doi.org/10.1016/j.icarus.2016.03.017

Hedman, M. M., & Nicholson, P. D. 2014, Monthly Notices of the Royal Astronomical Society, 444, 1369, doi: 10.1093/mnras/stu1503

Jerousek, R. G., Colwell, J. E., Hedman, M. M., et al. 2020, Icarus, 344, 113565, doi: 10.1016/j.icarus.2019.113565

Marouf, E. A., Leonard Tyler, G., Zebker, H. A., Simpson, R. A., & Eshleman, V. R. 1983, Icarus, 54, 189, doi: 10.1016/0019-1035(83)90192-6

Marouf, E. A., Tyler, G. L., & Rosen, P. A. 1986, Icarus, 68, 120

Murray, C. D., & French, R. S. 2018, The F Ring of Saturn, ed. M. S. Tiscareno & C. D. Murray, Cambridge Planetary Science (Cambridge University Press), 338–362

NASA/JPL-Caltech. 2004–2017, NASA/JPL Photojournal, https://photojournal.jpl.nasa.gov/

Wertheim, G. 1975, Journal of Electron Spectroscopy and Related Phenomena, 6, 239, doi: https://doi.org/10.1016/0368-2048(75)80019-3